Long wavelength analysis of Io's hotspots

G.J. van der Wel

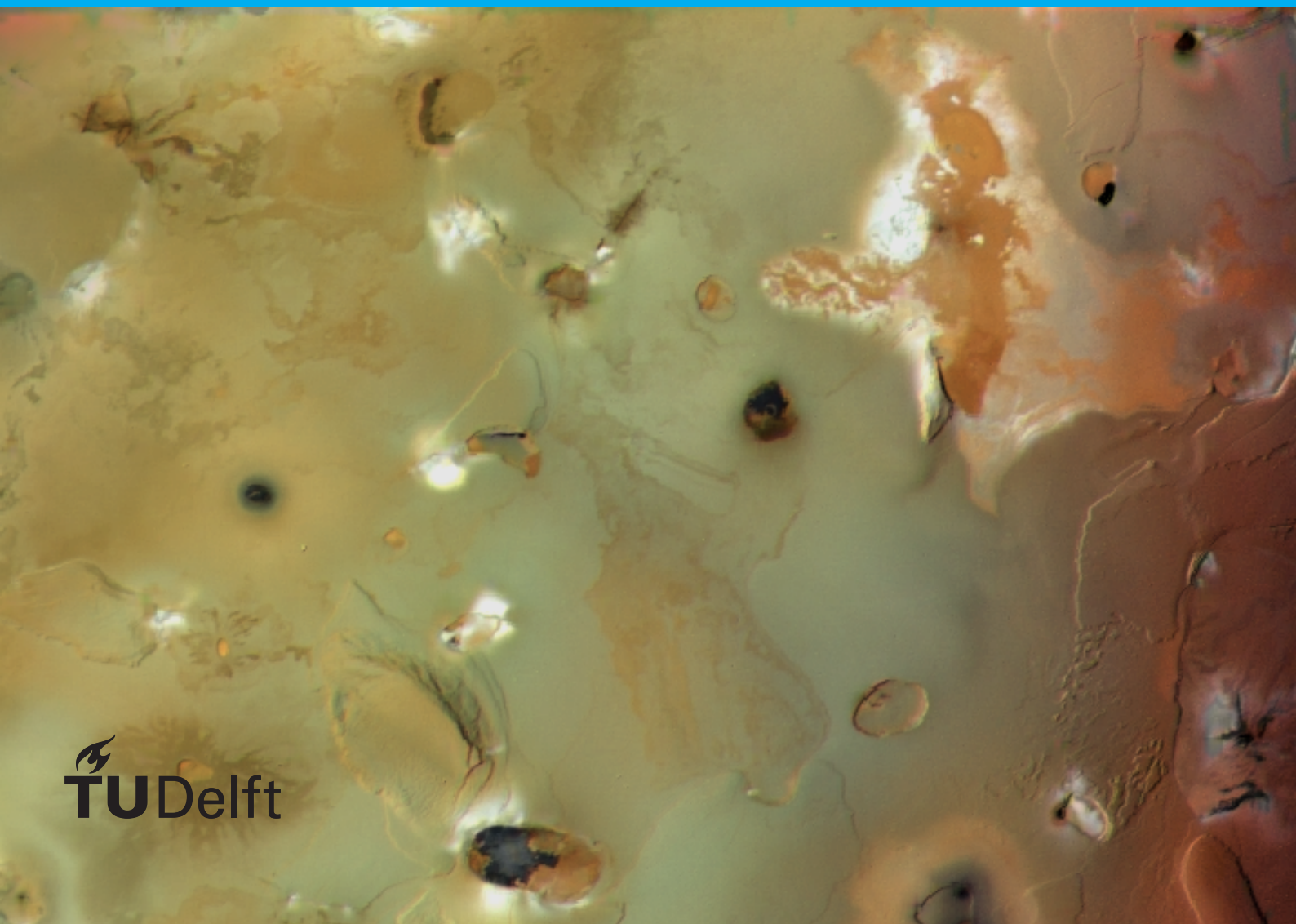

TU Delft

Long wavelength analysis of Io's hotspots

by

G.J. van der Wel

to obtain the degree of Master of Science
at the Delft University of Technology,
to be defended publicly on Thursday November 21, 2024 at 14:00 hours.

Student number:	1357409	
Project duration:	October 1, 2023 – November 21, 2024	
Thesis committee:	Dr. ir. E. Mooij,	TU Delft, Chair
	Dr. S. Paardekooper,	TU Delft, Examiner
	Dr. ir. W. van der Wal,	TU Delft, Thesis Supervisor
	Ir. A.K. Veenstra,	TU Delft, PhD Student

This thesis is confidential and cannot be made public until November 21, 2024.

An electronic version of this thesis is available at http://repository.tudelft.nl/.

Cover image depicts several volcanic centers on Io. Image courtesy of NASA/JPL/USGS at
https://science.nasa.gov/resource/io-erupts-3/

Contents

List of Figures

List of Tables

Acronyms

AO	Adaptive Optics
IRIS	InfraRed Interferometer Spectrometer
IRTF	InfraRed Telescope Facility
ISS	Imaging Science Subsystem
JIRAM	Jovian InraRed Auroral Mapper
LEISA	Linear Etalon Infrared Spectral Array
LORRI	LOng Range Reconnaissance Imager
NASA	National Aeronatics and Space Administration
NICMOS	Near Infrared Camera and multi-Object Spectrometer
NIMS	Near Infrared Mapping Spectrometer
NIRC2	Near-Infrared Camera, Second Generation
NIRI	Near-InfraRed Imager
PPR	PhotoPolarimeter-Radiometer
SH	Spherical Harmonics
SSI	Solid State Imager

List of Symbols

Symbol	Description	Unit
A	A correction factor indicative of the area represented by each point in a spherical harmonic field. This factor is the fraction of the total area over all latitudes that is represented by a combination of latitude and longitude coordinates.	$-$
c_{lm}	Spherical harmonic coefficient derived from θ_n and ϕ_n at degree l and order m	$-$
$c_{W,lm}$	Weighted spherical harmonic coefficient derived from θ_n and ϕ_n at degree l and order m	$-$, or GW
f_{lm}	Fully normalized spherical harmonic expansion at degree l and order m	$-$, or km^{-2}
$f_{W,lm}$	Fully normalized weighted spherical harmonic expansion at degree l and order m	$-$, or GW/km^2
l	Harmonic degree	$-$
P_{lm}	Legendre polynomial for degree l and order m; a complete system of orthogonal polynomials	$-$
m	Harmonic order; always satisfies the condition $0 \leq m \leq l$	$-$
n	Object index number	$-$
N	Total number of objects	$-$
R	Radius of Io; equal to ± 1821.6 (Lopes et al., 2023)	km
S_l^2	Spectral power at harmonic degree l	$-$
$S_{W,l}^2$	Weighted spectral power at harmonic degree l	$-$
s_{lm}	Spherical harmonic coefficient derived from θ_n and ϕ_n at degree l and order m	$-$
$s_{W,lm}$	Weighted spherical harmonic coefficient derived from θ_n and ϕ_n at degree l and order m	$-$, or GW
W	When used as a subscript it indicates the weighted version a spherical harmonic equation. When in a form like W_n this is the weight of object n; in this Thesis the hotspot intensity.	GW
δ	Kronecker delta; has to two indices (e.g. δ_{ij}) if both indices are identical the Kronecker delta equals 1, otherwise it equals 0	$-$
θ	Colatitude used to calculate the fully normalized spherical harmonics field	°
θ_n	Colatitude of object n; used to calculate c_{lm} and s_{lm}	°
λ_l	Wavelength corresponding to harmonic degree l	km
π	Ludolph's number; relates the circumference of circle to its radius	$-$
σ	Standard deviation	$-$
σ_l	Standard deviation for harmonic degree l	$-$
$\sigma_{W,l}$	Weighted standard deviation at harmonic degree l	$-$
ϕ	Longitude used to calculate the fully normalized spherical harmonics field	°
ϕ_n	Longitude of object n; used to calculate c_{lm} and s_{lm}	°

Summary

Jupiter's incredible mass in combination with Io's close proximity to the gas giant causes it to experience a massive build up of internal heat due to how much it is deformed. This in turn leads to Io being the most volcanically active body in the solar system (Pommier and McEwen, 2022). However, the exact make-up of Io's interior and how this leads to volcanism is unknown. Current observations still allow for the existence of several different models on how Io's heat is distributed across its interior (Lopes et al., 2023). A more complete understanding of Io's interior will also help model the conditions in and on exoplanets and exomoons that experience similar conditions.

In this Thesis, spherical harmonics applied to the hotspot distribution and intensity are used to identify long wavelength signals, because those can originate from deep within Io, thereby allowing a look into the interior of the moon. Spherical harmonics are used, instead of other methods such as nearest neighbor analysis, because spherical harmonics are particularly well suited to describe distributions on the surface of a sphere. One can think of it as Fourier analysis applied to the surface of a sphere. Previous research exists for different methods of finding long wavelength signals, such as gravity field measurements during flybys (Anderson et al., 2004) or examining Io's induced magnetic field (Khurana et al., 2011). This Thesis focuses on analyzing the hotspot distribution, similar to work performed by Kirchoff et al. (2011) and van Sliedregt (2020), but until now the intensity of the hotspots has not been included in these analyses. The result of the spherical harmonic analysis allows for the creation of maps showing the intensity distribution on the surface of Io, thereby allowing for a comparison with existing heat flux distribution maps.

By adding weights to the spherical harmonic expansion the impact of including hotspot intensities is examined, and both patterns represented by the weighted and unweighted spherical harmonics are compared to existing end-member models of Io's interior to determine if adding the intensity has an impact on which model is the best choice. These models are the Deep mantle heating model, where the source of Io's volcanism is located in the deep mantle; the Asthenospheric heating model where the magma is located closer to Io's surface; and the Magma Ocean model where there is a magma ocean directly under Io's surface; this model also has a variant where it's more of a Magmatic sponge (where magma is not entirely disaggregated), but its heat flux map is too similar to the Magma Ocean model to allow a distinction between these models using the work from this Thesis alone (Pater et al. (2021), Pommier and McEwen (2022) and Lopes et al. (2023)).

As only long wavelengths are relevant, the two strongest signals at low order harmonic degrees of the spherical harmonic expansion are investigated further. The first selected harmonic degree is $l = 2$ based on the spectral power of the unweighted spherical harmonic analysis. Additionally, this corresponds with the degree 2 signal found in existing works such as those by Kirchoff et al. (2011). The second selected harmonic degree is $l = 4$, because it produces the closest fit to the observed data when analyzing the hotspot distribution with and without intensity at low harmonic degrees. Interestingly, the spectral power of the weighted data has a strong signal at all harmonic degrees. The reason for this is that there is a large difference between the strongest source of Loki Patera and the next strongest hotspot, so a strong signal from Loki Patera is present in all lower degrees of the spherical harmonic expansion. This strong spectral power at all degrees (up to degree 30 has been checked) means one can take a low degree, such as 4, and argue that Loki Patera is a long wavelength phenomenon (supported by e.g. Veeder et al. (2009) and Veeder et al. (2011)), but it is equally valid to select a higher degree and argue Loki Patera is caused by a short range process such as ancient impacts and local rheology (mentioned by Steinke et al. (2020)). Unfortunately, this means that no definitive conclusion can be drawn as to whether the main signal found by the spherical harmonic analysis of Io's hotspot distribution, including the intensity, is a long wavelength signal originating from deep within Io.

Comparing the spherical harmonic fields at degree 2 and 4 with heat flow maps for the end-member models shows that both the hotspot distribution with and without intensity allow both the Asthenospheric or Magma ocean models as the source of Io's volcanism. Both the weighted and unweighted model show an offset to the east of the sub-Jovian and anti-Jovian point for the location of highest heat flow. This favors the Magma Ocean model, though a soon to be published article by Veenstra et al. (2024)

shows this offset also occurs in models without a magma ocean due to a feedback loop between tidal heating and melt generation. There is a major difference between the weighted and unweighted models, however, in that for the unweighted analysis the highest concentration of hotspots is at about 150 °W (30 °E of the anti-Jovian point), with a secondary maximum at about 330 °W just south of the equator (30 °E of the sub-Jovian point); in contrast the weighted analysis has the primary maximum near 315 °W just north of the equator with the secondary at about 150 °W only at harmonic degree 2 and no true secondary maximum for degree 4. This means that what appears to be the primary location for heat output of the hotspot distribution is not actually the location with the highest power output when considering the actual intensities.

For future research it may be worth investigating the possibility of mitigating the impact of a strong single source by dividing the power of hotspot over its emitting area, instead of keeping it focused on a single point. Although, the emitting area may still be too small compared to the total size of Io for this to make a large enough difference. Other potential avenues of research include using a smaller binsize when comparing the latitude and longitude distributions of the observations and the spherical harmonic models to see if that leads to a different fit between them, while making sure bins don't become too empty; investigating the hotspot power changes over time using the Veeder2015 (Veeder et al., 2015) and Davies2024 (Davies et al., 2024) data sets; or performing the spherical harmonic analysis on different types of volcanic location separately such as only dark paterae, bright paterae, outflows, etc., to see if they lead to similar results as the complete data set, because some types of hotspot may respond differently to local conditions or be caused by a different source. This does require calculating the emitted power for all hotspots that are currently missing it. One last recommendation is a dedicated satellite mission to Io capable of observing several physical parameters at once, such as magnetic induction, surface temperature and gravity field, because that will help constrain current models and allow further study of the heat output over time to definitively determine whether Io's volcanic activity varies (periodically) over time.

1 Introduction

Io is the most volcanically active body in the Solar system, even more so than Earth, because of its proximity to the gas giant of Jupiter. This leads to the moon being massively deformed due to Jupiter's gravitational pull, which results in a massive amount of thermal energy in the interior of the moon (Pommier and McEwen (2022), Lopes et al. (2023)). This energy is released via numerous powerful eruptions both short-lived and explosive, and longer-lived continuous outflows. An important question leading from this volcanic activity is how it is related to the interior of the moon. Unlike Earth where the interior make-up, while still being discovered in detail (Phạm and Tkalčić (2023)), is roughly known, the same cannot be said of Io. There are still several possible models based on current observations of Io's hotspots and limited availability of gravitational measurements (e.g. Lopes et al. (2023) and Davies and Veeder (2023)). Understanding the interior of Io will lead to a greater understanding of the interior and exterior conditions on extra-solar bodies that share similar circumstances.

In order to find out more about the interior of Io one can look for long wavelength patterns on Io, because the long wavelength means the cause of the phenomenon being observed is most likely located deep within the moon. There is no indication in existing literature of long wavelength signals not originating from deep inside Io. Existing long wavelength analysis includes observations of its gravity field during flybys (Anderson et al., 2004) to restrain the make-up and size of Io's core, and examining its induced magnetic field to find that Io's mantle cannot be completely solid (Khurana et al., 2011). Looking at Io's hotspots specifically, Kirchoff et al. (2011) uses spherical harmonics to analyze the global distribution of mountains and volcanic centers on Io and found that these are likely caused by asthenospheric (upper part of the mantle right under the crust) heating. Hamilton et al. (2013) uses Nearest Neighbor (NN) analyses on the hotspot distribution to find that deep mantle heating fits a global NN analysis and asthenospheric heating (with a 30-60° offset from the model) when considering the near-equatorial concentration of volcanism. Veeder et al. (2012) shows a shift to the east from predicted heat flow patterns for the asthenospheric tidal heating model, and Davies et al. (2015) created maps of the global heat flow based on Io's hotspots to conclude neither the deep mantle heating model, the asthenospheric heating model, or any combination thereof examined at the time can explain observed heat flow patterns.

This Thesis will expand on the use of using spherical harmonics, such as used by Kirchoff et al. (2011) and van Sliedregt (2020), because they are a type of function particularly well-suited for describing distributions on a sphere. These functions can be thought of as a Fourier series applied to the surface of a sphere (Sneeuw (1994)), and allow one to create models showing the concentrations of hotspots at different wavelengths. One can also use the spectral power of these wavelengths to determine which wavelength best describes the hotspot distribution. This Thesis expands on existing work by adding the hotspot intensity to the hotspot distribution by modifying the spherical harmonic equations to include a weighting factor. This weighting factor can also be used to add different information, but only the hotspot intensity is considered here. Including this information could potentially uncover new patterns that can not be gleaned from the distribution of hotspots alone. To do this the assumption is used that any long-wavelength signals discovered are the result of planetary scale heat redistribution in the interior of the moon. This is a logical assumption to make, because otherwise the large amount of heat generated by Jupiter's proximity and Io's eccentricity would have to be generated

mostly, if not entirely, in the uppermost part of Io's interior close to the crust. That makes little sense given the entire moon is affected the deformation caused by Jupiter's proximity and Io's eccentricity. The spherical harmonic results are also compared to existing work to verify the method has been implemented correctly. The weighted and unweighted spherical harmonic fields produced by the spherical harmonic expansion will also be compared to existing end-member models.

The Thesis is structured as follows. Chapter 2 on page 3 gives a brief overview of the currently available observations of Io, the suggested models for its internal heat distribution, and a short look at Io's biggest hotspot. Chapter 3 on page 9 provides more details on the (un)weighted spherical harmonics, such as the equations used in this Thesis. Chapter 4 on page 15 verifies the (weighted) spherical harmonics work as intended by comparing the results produced for this Thesis to existing work. Chapter 5 on page 17 details the data sets used in this chapter, the best spherical harmonic degrees to use and analyses the results of the unweighted and weighted spherical harmonics. The last chapter of this Thesis is Chapter 6 on page 33, which are the conclusions and recommendations.

2

Observation of hotspots and modelling the interior of Io

Io is a unique planetary body in the Solar system and one can explore its properties using many different means, such as magnetic (Khurana et al., 2011) or gravitational measurements (Anderson et al., 2004), or determining the amount and type of volcanic material ejected into orbit around Jupiter (Pater et al., 2020). This Thesis focuses primarily on further restricting the possible interior structure of Io using the heat flow based on (the intensity of) volcanic activity. Section 2.1 gives a brief overview of the history of Io observations, with a focus on detecting volcanic eruptions. After that, Section 2.2 on page 4 goes into detail on the existing types of models that may explain Io's interior structure. Section 2.3 on page 8 briefly discusses the potential source of Io's most famous and outstanding hotspot, Loki Patera.

2.1. A brief overview of remote observations of hotspots on Io

Io was first discovered in 1610 independently by both Galileo Galilei and Simon Marius, along with the three other Galilean moons of Europa, Ganymede and Callisto. While Io has been observed in the centuries since, discovering, for example, the 4:2:1 orbital resonance between Io, Europa and Ganymede, and deriving enough information to conclude Io must be a rocky planet (Pommier and McEwen (2022), Lopes et al. (2023)), Io's potential for volcanism wasn't officially proposed until 1979 by Peale et al. just a few days before Voyager I entered the Jupiter system (Peale et al., 1979). In their paper they predicted that Io's interior might melt due to tidal heating caused by Io's extreme proximity to Jupiter and the forced eccentricities caused by the resonance with the other Galilean moons. Their prediction would turn out to be accurate, in fact it is estimated that Io's total thermal emission is ± 105 TW, about half of which is emitted by Io's volcanoes (Davies et al., 2024).

Io's volcanism is similar to some of Earth's. More specifically, the volcanoes on Io show similarities to some of the basaltic volcanoes found in Hawaii. In contrast to Earth, Io, while having mountains up to ± 18 km high (Kirchoff et al., 2011), does not possess any stratovolcanoes. So far, remote observations have confirmed the presence of silicate lavas, and there are a few observations which point to ultramafic lava (lava very low in silicates with a very high melting point at over 1200 °C), but this is not yet definitive (Pater et al., 2021). Most volcanic centers on Io have dark circular features surrounding them and are lower than the surrounding terrain. So because this makes them look somewhat like calderas on Earth and this appearance isn't necessarily due to volcanic processes, these volcanic centers are usually referred to with 'patera' ('paterae' for plural) (Lopes et al., 2023).

Unfortunately, no dedicated mission to Io has been launched so far due to the extremely inhospitable conditions caused by the intense radiation from Jupiter's magnetic field (Pommier and McEwen, 2022), but a lot of information has been gained by satellites doing a flyby of Jupiter or Io, and by satellites observing Io after their main mission is completed, such as Galileo and Juno (e.g. NASA (2009), Mura et al. (2020) and Zambon et al. (2023)). The rest of this section will highlight the main instruments used to observe hotspots that have erupted recently, and those that were active but haven't cooled enough for a layer of sulfur to form over the hotspot location. Io's consistent volcanic eruptions lead to rapid resurfacing (geologically speaking) so hotspot locations that have been inactive for too long (± 1 million

years) cannot be detected, because they've been covered by volcanic ejecta (Williams et al. (2011) and Hamilton et al. (2013)).

Some of the instruments used to study Io's thermal output over the years, starting with the Voyager I mission will be mentioned here. The Voyager I mission passed by the Jovian system and managed to make several images of Io using its Imaging Science Subsystem (ISS) and InfraRed Interferometer Spectrometer (IRIS) subsystems. By combining the Voyager I ISS images with data obtained using Galileo's Solid State Imager (SSI), Williams et al. (2011) was able to create a global geologic map of Io. Galileo's observations of Io after completion of its primary mission using its PhotoPolarimeter-Radiometer (PPR) and Near Infrared Mapping Spectrometer (NIMS) instruments yielded an extensive amount of data about Io's thermal emissions being used by the scientific community to this day (Davies et al. (2015) and NASA and JPL-Caltech (2023) among many others). In a similar fashion, Juno's Jovian InraRed Auroral Mapper (JIRAM) instrument has been used sporadically during Juno's primary mission to study Io's heat output, and is still being used now that Juno's primary mission has been completed (Mura et al. (2020) and Zambon et al. (2023)). Fly-by missions have also yielded some data on Io's thermal activity, such as New Horizon's LOng Range Reconnaissance Imager (LORRI) and Linear Etalon Infrared Spectral Array (LEISA) instruments, and Cassini's ISS subsystem (Veeder et al. (2015) and Hamilton et al. (2013)). There even exist a few observations using Hubble's Near Infrared Camera and multi-Object Spectrometer (NICMOS) instrument (Hamilton et al., 2013). There also exist many earth-based observations of Io's stronger hotspots thanks to the advent of Adaptive Optics (AO) allowing for corrections caused by distortions from Earth's atmosphere. The main observatories delivering data about Io's heat flow are all based in Hawaii and are the Keck Observatory using its Near-Infrared Camera, Second Generation (NIRC2) instrument, the Gemini N Observatory using its Near-InfraRed Imager (NIRI) instrument, and the Mauna Kea Observatory using its InfraRed Telescope Facility (IRTF) instrument (Davies et al. (2015) and de Kleer et al. (2019b)).

In Chapter 5 data obtained from the above mentioned sources is used. For information on how this data is processed and used, see Section 5.1 on page 17.

2.2. Existing models for Io's internal structure

That Io is a volcanically active moon is without question in the current day, but the exact interior structure of Io is still an unknown. The current assumption is that Io has a Fe-FeS core of about 950 km radius and a silicate based mantle and asthenosphere (Pommier and McEwen, 2022). Due to Io supporting some very impressive mountains of up to ± 18 km, it needs to have a thick silicate crust to support those mountains (Kirchoff et al., 2011). Io's high volcanic activity also means it has some amount of melt, but the amount and location of this melt (if it's in a melt layer, or pockets, and at what depth) is still uncertain.

There currently exist three end-member models of Io's interior structure, one of which can be split into two separate but similar models. Note that models are referred to as end-member models, because they are likely an oversimplification of reality. The three main models, as illustrated in Figure 2.1 on page 5, are the deep mantle heating model (A), the asthenospheric heating model (B), and the magma ocean model. This last model is then split in a pure magma ocean (D) and a magmatic sponge model (C) (Lopes et al. (2023), Pommier and McEwen (2022) and Pater et al. (2021)). In the deep mantle heating model (A) it is assumed that the volcanism arises from solid body heat dissipation in the deep mantle, so there is no significant melt layer. The asthenospheric heating model (B) is similar, but here it is assumed the heat is dissipated in the asthenosphere, so closer to the surface of Io. In the magma ocean model (D) (Tyler et al., 2015) there is a liquid magma ocean between the asthenosphere and crust. The necessity of the magma ocean for certain observations is still unclear with research available supporting this model (Šebek et al., 2019) and research that can explain certain measurements without the need for a magma ocean, such as the magnetic induction (Blöcker et al., 2018) and the eastward offset of the highest concentrations of heat away from sub- and anti-Jovian points (see an upcoming article by Veenstra et al. (2024)). As it stands, the magma ocean model is a viable option. The magma sponge model (C) is similar to the magma ocean model, but instead of being completely disaggregated the melt is still contained within a solid silicate medium. See Figure 2.2 on page 5 for different forms that melt could take within Io; de Kleer et al. (2019b) goes into more detail on this matter.

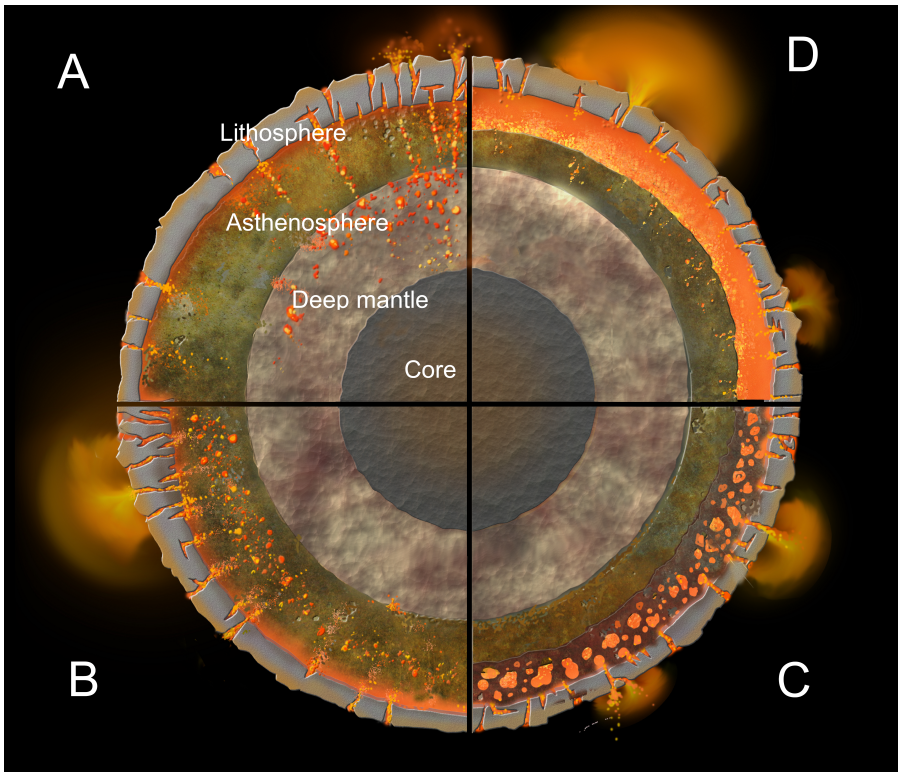

Figure 2.1: A schematic depiction of the interior structure of Io for the four different end-member models, counterclockwise from the top-left: solid body dissipation in the deep mantle (A), solid body dissipation in the asthenosphere (B), dissipation in a magmatic sponge (C), and fluid body dissipation in a magma ocean (D). See Table 2.1 on page 6 for a comparison of how the geophysical properties of Io are affected by the different models. Note that the features in this image are not to scale. Edit of an image courtesy of Chuck Carter and James Tuttle Keane / Keck Institute for Space Studies (Chatila (2024)).

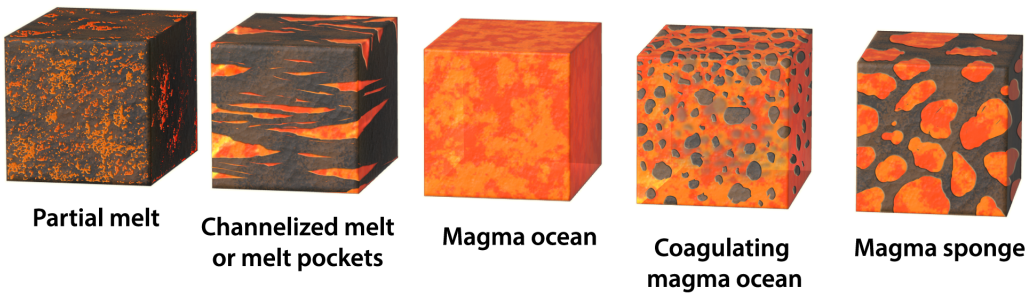

Figure 2.2: This image shows the potential physical form melt can take inside Io and other similar partially molten exoplanets. Image scale is in the order of about one centimeter. Image courtesy of Chuck Carter and James Tuttle Keane / Keck Institute for Space Studies (Chatila (2024)).

These different models give rise to different physical properties. So by measuring certain geophysical properties the most accurate type of model can be found. The geophysical properties for the different end-member models are listed and compared in Table 2.1. The analysis presented in this Thesis will focus primarily on the heat flux distribution by using spherical harmonics to produce a model showing the power output per square kilometer.

Table 2.1: The geophysical measurements corresponding to each of the four end-member models for Io's interior structure. This table is a copy of Table 4.4 on page 140 from Lopes et al. (2023).

	A Solid Io, with dissipation in the deep mantle	**B** Solid Io, with dissipation in the asthenosphere	**C** Io with a magma ocean	**D** Io with a magma "sponge"
Tidal deformation (e.g. k_2)	Low	Low	High	Low
Libration amplitude	Small	Small	Large	Small
Magnetic induction	Weak	Weak	Strong	Strong
Lava temperature	High-temperature basaltic	Basaltic	Very high-temperature ultramafic	Very high-temperature ultramafic
Heat flux distribution	More polar	More equatorial	More equatorial or uniform	More equatorial or uniform
Crustal thickness variations	Thin at equator	Thin at pole	Uniform	Uniform

For an overview of how the heat flux looks like on a planetary level, as opposed to the simple description given in Table 2.1, see Figure 2.3 on page 7. Similar figures can be found across the scientific literature discussing the interior structure of Io. For deep mantle heating (A) you can clearly see the concentration of heat on the poles mentioned in Table 2.1, but based purely on Table 2.1 the presence of strong minima centered on the sub- and- anti-Jovian point could be overlooked. For the asthenospheric heating (B) there are minima on the poles, as expected based on Table 2.1, and the maxima are located at the sub-Jovian and anti-Jovian points, but not directly on the equator, instead just to the North and South of it. The asthenospheric heating model also has secondary maxima between the sub- and- anti-Jovian points on the equator. The magma ocean and magma sponge models (C in Figure 2.3) show heat flow primarily focused around the equator where the maxima are actually located on the equator, unlike for the asthenospheric heating model, and have their maxima shifted to the east of of the sub- and- anti-Jovian points.

Because the end-member models have sufficiently different heat distribution on the surface to be clearly unique from each other, this helps determine which model is the best fit for results of the weighted and unweighted spherical harmonics, based on the location of highest heat flow using both the North-South and East-West differences in the end-member models. The only exception is the Magma Ocean and Magma Sponge models whose heat distribution is too similar to separate based solely on that, so only the Magma Ocean model will be taken into account. As each model corresponds to a different internal structure, the best model is most likely to represent the real interior structure of Io. These best fits are determined in Section 5.3 on page 25 and Section 5.4 on page 27.

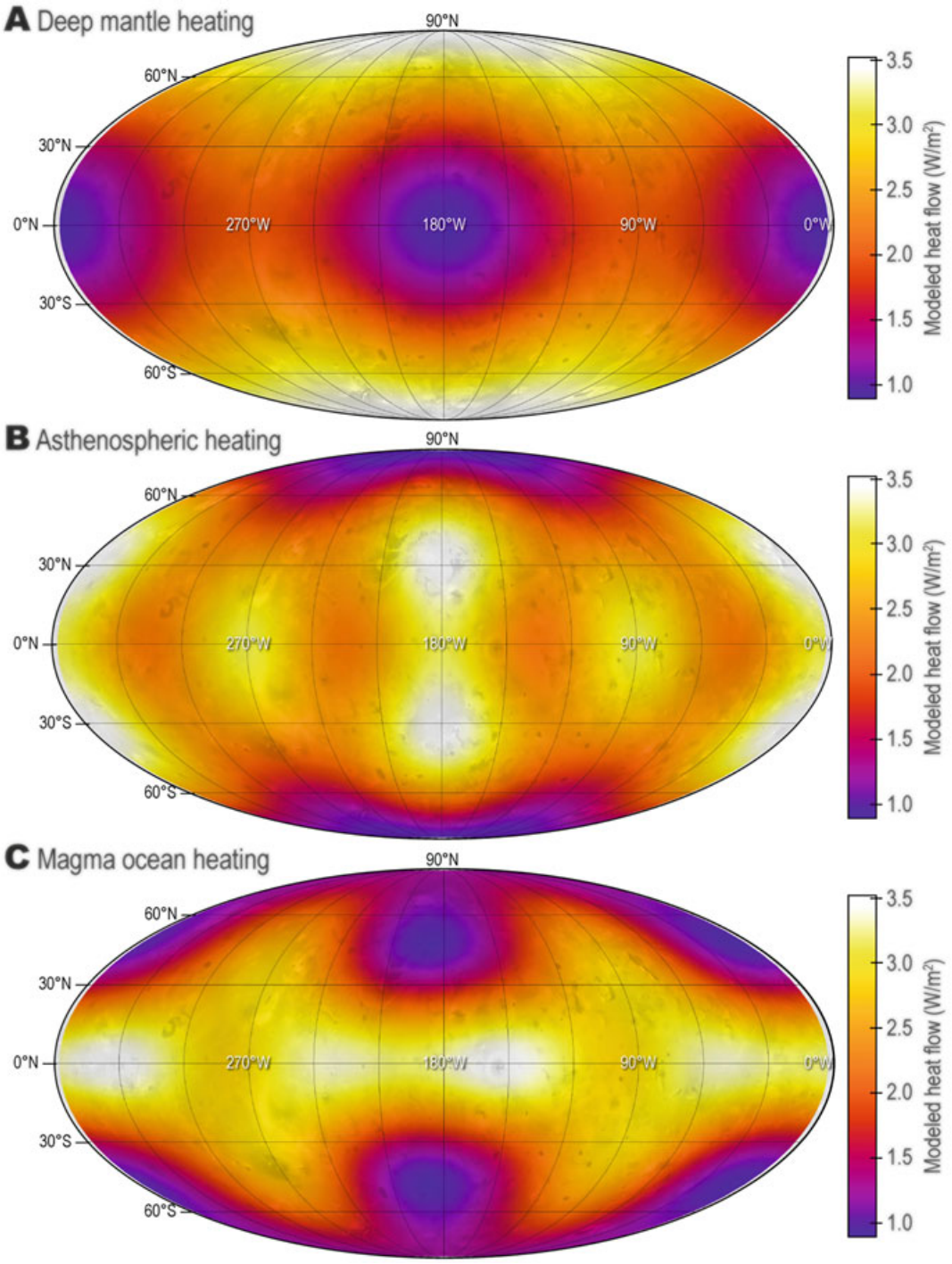

Figure 2.3: Modeled heat flow at the surface of Io caused by tidal dissipation within Io, for three of the end-member models. The top image shows the result of tidal heating concentrated solely in the deep mantle, the middle image shows the result of tidal heating purely in the asthenosphere, and the bottom image shows the result of tidal heating purely in a magma ocean. Image is a copy of Figure 4.3 on page 115 of Lopes et al. (2023); for detailed properties of these models see Table 4.1 of Lopes et al. (2023).

2.3. The potential origins of Loki Patera

The most famous hotspot on Io is Loki Patera at 10 °N and 310 °W, because of its massive size (> 200 (km) diameter (Radebaugh et al., 2001)) and heat output. In fact, it is in and of itself responsible for ± 10% of Io's total heat output (Veeder et al., 2012), or one fifth of the total volcanic heat flow. Because of it's massive power Loki is expected to have noticeable impact on the spherical harmonic analysis when taking into account the hotspot intensities.

It is still unknown why Loki Patera is so massive, and what exactly the cause is for this standout feature on the surface of Io. Due to its massive heat output one might expect this hotspot to be caused by some sort of global process. For example, when looking at the heat flow from all dark patera (which Loki is one of) this heat flow is centered around Loki with another concentration of heat roughly as strong directly opposite of Loki Patera on Io's other hemisphere (Veeder et al., 2011). Similarly, studying the flow from dark fields (which Loki is not part of) shows that most of the heat from dark fields is found on the hemisphere opposite of Loki Patera (Veeder et al., 2009). From these two studies one certainly gets the impression there is some sort of global process balancing heat across the surface of the moon. On the other hand, one can argue Loki Patera is the product of a local phenomenon, perhaps an asteroid or meteorite impact sufficiently weakened the surface to allow the creation of Loki Patera (and perhaps other hotspots), or the local rheology combined with mantle upwellings creates Loki (Steinke et al., 2020).

3

Identifying long wavelength features using spherical harmonics

Long wavelength features can be used to determine, or at least narrow down, Io's interior structure, unlike short-wavelength signal which are related to more local phenomena on or close to Io's surface. In this Thesis the distribution and intensity of hotspots are analyzed using spherical harmonics to find long wavelength signals.

Some other methods that have been used to find long wavelength features include using nearest neighbor analysis (Hamilton et al., 2013), putting the intensity into bins across Io's latitude and longitude (Veeder et al. (2012), Veeder et al. (2015)) and creating contoured maps using those bins (Davies et al., 2015), or using spherical harmonics (Kirchoff et al., 2011). For this Thesis spherical harmonics were chosen, because it is an excellent way to quantitatively analyze distributions on a sphere, and the models produced by the spherical harmonic analysis can themselves be divided into bins across latitude and longitude, such as those used by Davies et al. (2024) for easy comparison. It is also a convenient way to study hotspot distributions for several wavelengths and determining which is the best fit to existing data. This Thesis continues earlier work by Kirchoff et al. (2011) and van Sliedregt (2020) by adding weights to the spherical harmonic analysis to include the power of hotspots.

Spherical harmonics analysis can be considered as applying a Fourier analysis to the surface of a sphere. In this Thesis spherical harmonics are used to find long wavelength signals in the distribution of volcanic hotspots on the surface of Io, as well as identify long-wavelength signals in the intensity distribution of volcanic hotspots. Existing literature, such as Veeder et al. (2012), Steinke et al. (2020) and Davies and Veeder (2023), contain analyses of the global surface pattern and intensity of Io's hotspots and mention these are the result of planetary scale heat distribution in the interior of Io. So any long wavelength signals found in this Thesis are also taken to be from the interior of Io.

This chapter is split into three parts, Section 3.1 elaborates on the equations used for the unweighted spherical harmonics, Section 3.2 on page 11 shows the required to changes to perform spherical analysis with weights (so the hotspot intensity can be incorporated), and Section 3.3 on page 13 details how the equations from the previous two sections have been applied to Io's hotspots.

3.1. Spherical harmonics

The fully normalized spherical harmonic field is calculated using:

$$f_{lm}(\theta,\phi) = \sqrt{\frac{(2-\delta_{0m})\,(2l+1)\,(l-m)!}{4\pi\,(lm)!}} P_{lm}(\cos\theta)\,(c_{lm}\cos m\phi + s_{lm}\sin m\phi) \tag{3.1}$$

Here f_{lm} is the spherical harmonic field for harmonic degree l and order m, where m satisfies $0 \leq m \leq l$. P_{lm} are the associated Legendre polynomials at degree l and order m. θ is the colatitude, ϕ is the longitude, c_{lm} and s_{lm} are the harmonic coefficients derived from colatitude and longitude of surface distribution (hotspots). δ_{ij} is the Kronecker delta function, which is 1 if both indices are identical and 0 otherwise. This equation is a copy of Equation 1 from Kirchoff et al. (2011).

The spherical harmonic coefficients, c_{lm} and s_{lm}, are:

$$c_{lm} = \sqrt{\frac{(2-\delta_{0m})\,(2l+1)\,(l-m)!}{4\pi\,(lm)!}} \sum_{n=1}^{N} P_{lm}\,(\cos\theta_n)\cos m\phi_n$$
$$s_{lm} = \sqrt{\frac{(2-\delta_{0m})\,(2l+1)\,(l-m)!}{4\pi\,(lm)!}} \sum_{n=1}^{N} P_{lm}\,(\cos\theta_n)\sin m\phi_n \tag{3.2}$$

Here θ_n is the colatitude of object of interest n and ϕ_n is the longitude of the same object. The objects can be anything worth studying, but for this Thesis they are the locations of hotspots; for more details on how the equations in this section are applied to the subject of this Thesis, see Section 3.3 on page 13. N is the total number of objects (hotspots in the case of this Thesis). This equation is a copy of Equation 2 from Kirchoff et al. (2011)

The spherical harmonic coefficients can be used to find the spectral power S_l^2 of the distribution being studied:

$$S_l^2 = \frac{4\pi}{N\,(2l+1)} \sum_{m=0}^{l} \left({c_{lm}}^2 + {s_{lm}}^2\right) \tag{3.3}$$

This is a copy of Equation 3 from Kirchoff et al. (2011). The spectral power is used to determine if there is a strong signal at a harmonic degree l. A completely random distribution of objects on a sphere will produce a spectral power at all degrees equal to 1. So a value different enough from unity indicates that there is a physical process behind the distribution. To find whether this difference from unity is large enough, the standard deviation at each degree is used to determine whether the signal is statistically significant. This standard deviation is given by:

$$\sigma_l = \sqrt{\frac{2\,(N-1)}{N\,(2l+1)}} \tag{3.4}$$

This is a copy of the in-line equation in the first paragraph on page 4 of Kirchoff et al. (2011). The standard deviation per degree is an indication of the likelihood the spectral power is the result of a non-random distribution of points (hotspots) at that harmonic degree l. A spectral power equal to positive or negative $1\sigma_l$ equals ± 68% confidence the distribution is non-random, at positive or negative $2\sigma_l$ it's 95% confidence, etc.

Using Equations (3.1) and (3.2) the spherical harmonic field can be calculated for each degree, and with Equations (3.3) and (3.4) the strength of the signal for a certain degree and the likelihood of it being caused by a non-random physical process can be determined. For the complete picture one would need to run the spherical harmonic analysis up to infinity, but obviously this is impractical. For this Thesis there is a practical limit due to the fact only signals caused by Io's internal processes are of interest, meaning only long wavelengths are relevant. It is possible to translate from wavelength to harmonic degree, because the moons circumference is related to the wavelength of a harmonic degree via:

$$\lambda_l = \frac{2\pi R}{l} \tag{3.5}$$

Here R is the radius of Io and λ_l is the wavelength at degree l. To satisfy the long wavelength requirement the spherical harmonic expansion is truncated at the last degree greater than or equal to the order of magnitude of the radius of Io, so at 1000 kilometers, which turns out to be at l = 11. Section 5.2 on page 21 goes into more detail on why this harmonic degree can be set to a higher degree without significantly changing the conclusions.

For the purposes of this Thesis the equations given by Kirchoff et al. (2011) are slightly modified similar to what is done in Section 2.3 of van Sliedregt (2020). For the spherical harmonic coefficients, the normalization is adapted such that the value of C_{00} is equal to the average number of data points per unit area of a unit sphere ($C_{00} = N/4\pi$). So the new versions of the spherical harmonic coefficients are now given by:

$$c_{lm} = \frac{1}{4\pi}\sqrt{\frac{(2-\delta_{0m})\,(2l+1)\,(l-m)!}{(lm)!}}\sum_{n=1}^{N} P_{lm}\,(\cos\theta_n)\cos m\phi_n$$
$$s_{lm} = \frac{1}{4\pi}\sqrt{\frac{(2-\delta_{0m})\,(2l+1)\,(l-m)!}{(lm)!}}\sum_{n=1}^{N} P_{lm}\,(\cos\theta_n)\sin m\phi_n \tag{3.6}$$

This, in turn, changes the equation for the spherical harmonic field. However, an additional change is made to this field to ensure the unit of the field is the number of hotspots per square kilometer (km^{-2}). This allows for convenient interpretation of results in Chapter 5. Additionally, the average number of points per square kilometer is then easily determined by finding the value of the field f_{lm} at degree and order 0 (that field is a constant value). This additional change is achieved by dividing the whole equation by the square of the radius of Io:

$$f_{lm}\,(\theta,\phi) = \frac{1}{R^2}\sqrt{\frac{(2-\delta_{0m})\,(2l+1)\,(l-m)!}{(lm)!}}P_{lm}\,(\cos\theta)\,(c_{lm}\cos m\phi + s_{lm}\sin m\phi) \tag{3.7}$$

R is the radius of Io. Comparing this equation with Equation (3.1) shows that the result of changing the spherical harmonic coefficients is the removal of the 4π term under the square root.

The equation to find the spectral power has to be adjusted as well to ensure a random distribution of objects on a sphere still results in a mean of unity for the spectral power for all degrees. So Equation (3.3) is replaced by:

$$S_l^2 = \frac{(4\pi)^2}{N\,(2l+1)}\sum_{m=0}^{l}\left({c_{lm}}^2 + {s_{lm}}^2\right) \tag{3.8}$$

The standard deviation given by Equation (3.4) remains unchanged. While the division by the radius of Io could have been included with the normalization of the spherical harmonic coefficients, allowing one to find the average number of points per square kilometer by simply looking at the c_{lm} coefficient at degree and order 0, by not doing this, the coefficients are easier to parse by eye. On a related note, this change would then also have to be included in the calculation for the spectral power, but this will then lead to the exact same result as obtained by the equations above. So the radius is only included in the normalization for the field, mostly as matter of convenience.

3.2. Weighted spherical harmonics

One of the goals of this Thesis is to incorporate the intensity measured at hotspots when performing a spherical analysis. In order to do this weights are added to each hotspot, and these weights are the measured intensity in gigawatts (GW). The equations for spherical harmonics with weights are taken from Kirchoff et al. (2011), just like the equations for spherical harmonics without weights.

The weighted spherical harmonic coefficients are created by combining information from the second paragraph on page 4 and Equation 2 from Kirchoff et al. (2011):

$$c_{W,lm} = \sqrt{\frac{(2-\delta_{0m})\,(2l+1)\,(l-m)!}{4\pi\,(lm)!}}\,\frac{\sum_{n=1}^{N} W_n P_{lm}\,(\cos\theta_n)\cos m\phi_n}{\sum_{n=1}^{N} W_n}$$
$$s_{W,lm} = \sqrt{\frac{(2-\delta_{0m})\,(2l+1)\,(l-m)!}{4\pi\,(lm)!}}\,\frac{\sum_{n=1}^{N} W_n P_{lm}\,(\cos\theta_n)\sin m\phi_n}{\sum_{n=1}^{N} W_n} \tag{3.9}$$

Here $c_{W,lm}$ and $s_{W,lm}$ are the weighted spherical harmonic coefficients. W_n are the weights, which in the case of this Thesis is the measured intensity at each volcanic location. For more information on variables not detailed in this section, refer to Section 3.1.

The spherical harmonic field with weights, $f_{W,lm}$, is derived from the second paragraph on page 4 and Equation 1 from Kirchoff et al. (2011):

$$f_{W,lm}(\theta,\phi) = \sqrt{\frac{(2-\delta_{0m})(2l+1)(l-m)!}{4\pi(lm)!}} P_{lm}(\cos\theta)\left(c_{W,lm}\cos m\phi + s_{W,lm}\sin m\phi\right) \tag{3.10}$$

The weighted spectral power, $S^2_{W,l}$ is derived from Equation 3 and information form the second paragraph on page 4 of Kirchoff et al. (2011):

$$S^2_{W,l} = \frac{4\pi}{N(2l+1)} \sum_{m=0}^{l} \left({c_{W,lm}}^2 + {s_{W,lm}}^2\right) \frac{\left(\sum_{n=1}^{N} W_n\right)^2}{\sum_{n=1}^{N} W_n^2} \tag{3.11}$$

The standard deviation at degree l, $\sigma_{W,l}$, is given by Equation 4 from Kirchoff et al. (2011):

$$\sigma_{W,l} = \sqrt{\frac{2}{(2l+1)\left(\sum_{n=1}^{N} W_n^2\right)^2} \sum_{j=1}^{N}\sum_{k=1}^{N} \left(1-\delta_{jk}\right) W_j^2 W_k^2} \tag{3.12}$$

Like the unweighted spherical harmonic equations, the weighted equations are adapted similar to Section 2.3 of van Sliedregt (2020). The normalization of the weighted spherical harmonic coefficients are changed so that the average number of data points per unit area of a unit sphere is given by $C_{00} = N/4\pi$. As a result the adapted weighted spherical harmonic coefficients, $c_{W,lm}$ and $s_{W,lm}$, are:

$$\begin{aligned} c_{W,lm} &= \frac{1}{4\pi}\sqrt{\frac{(2-\delta_{0m})(2l+1)(l-m)!}{4\pi(lm)!}} \sum_{n=1}^{N} W_n P_{lm}(\cos\theta_n)\cos m\phi_n \\ s_{W,lm} &= \frac{1}{4\pi}\sqrt{\frac{(2-\delta_{0m})(2l+1)(l-m)!}{4\pi(lm)!}} \sum_{n=1}^{N} W_n P_{lm}(\cos\theta_n)\sin m\phi_n \end{aligned} \tag{3.13}$$

The weighted spherical harmonic field, $f_{W,lm}$, is adapted to take into account the changes to the weighted spherical harmonic coefficients. It is further altered to have the unit of (GW/km^2) by dividing it by the square of the radius of Io, and removing the sum of all weights in the divisor. Thanks to these additional alterations the resultant field is in a unit that allows for easy interpretation in Chapter 5. As an added bonus the average power per square kilometer is easily determined by finding the value of the field $f_{W,lm}$ at degree and order 0 (that field is a constant value). As a result of the above mentioned alteration the new equation for the weighted spherical harmonic field is:

$$f_{W,lm}(\theta,\phi) = \frac{1}{R^2}\sqrt{\frac{(2-\delta_{0m})(2l+1)(l-m)!}{4\pi(lm)!}} P_{lm}(\cos\theta)\left(c_{W,lm}\cos m\phi + s_{W,lm}\sin m\phi\right) \tag{3.14}$$

As mentioned earlier in this section, refer to Section 3.1 for more information on variables not detailed here.

Due to the changes in the weighted spherical harmonic coefficients, the weighted spectral power, $S^2_{W,l}$, is changed as well:

$$S^2_{W,l} = \frac{(4\pi)^2}{N(2l+1)} \sum_{m=0}^{l} \left({c_{W,lm}}^2 + {s_{W,lm}}^2\right) \frac{\left(\sum_{n=1}^{N} W_n\right)^2}{\sum_{n=1}^{N} W_n^2} \tag{3.15}$$

The only change to the weighted spectral power is to ensure that the power at each degree for a random distribution of points a sphere is equal to unity. To check whether the difference from unity in the weighted spectral power is significant, the standard deviation per degree is calculated using Equation (3.12). The relation between harmonic degree and wavelength given by Equation (3.5) applies unchanged to the weighted equations.

3.3. Implementing the equations numerically

Now that the theoretical base has been established this section will describe how these equations are applied to the hotspot distribution of Io.

In order to calculate the spherical harmonic field, the spherical harmonic coefficients given by Equation (3.6) have to be calculated first. The Legendre polynomials are calculated using the 'plm' Matlab function created by Sneeuw (Sneeuw, 1994). So the remaining inputs are the location of all hotspots, which are given in (or converted to) colatitude θ_n and longitude ϕ_n, and the maximum harmonic degree l up to which the spherical harmonics will be computed. Io's hotspot distribution only consists of several hundred locations (see Section 5.1), so the coefficients are calculated incredibly quickly even up to a fairly high degree of 30. This number is chosen rather arbitrarily, but it is well beyond any long-wavelength signals. Any excess information based on the optimal cut-off point can be easily ignored or discarded later.

With the spherical harmonic coefficients known, the spherical harmonic field f_{lm} is calculated for each degree l and order m up to the cut-off value for l. A field is defined as a set of 181 x 360 points, one for each degree of latitude and longitude (181 for latitude, to ensure both poles are included). These fields are then combined and saved for each harmonic degree, to be plotted or otherwise processed later. Using the spherical harmonic coefficients, the spectral power (Equation (3.8)) and corresponding standard deviation (Equation (3.4)) can also be determined.

In order to take into account the hotspot intensities, the spherical harmonic equations with weights from Section 3.2 are used. The process is very similar, but instead of supplying only the colatitude θ_n and longitude ϕ_n, the intensities are supplied as W_n. By substituting these into Equation (3.13) the weighted spherical harmonic coefficients are calculated. With the weighted spherical harmonic coefficients known the spherical harmonic field can be calculated using Equation (3.14), the spectral power using Equation (3.15) and the standard deviation using Equation (3.12).

Now that the data up to a degree much higher than needed for long wavelengths is present (harmonic degree 30 corresponds to a wavelength of only ± 382 (km), a.k.a. 1/30 of Io's circumference), the optimal degrees to find long wavelength signals can be determined. This is discussed further in Section 5.2 on page 21.

4

Verifying the weighted and unweighted spherical harmonic expansion

This chapter includes some tests to check if the spherical harmonic expansion works as intended for data with and without weights. The unweighted spherical harmonics are tested in Section 4.1 by comparing one of the data sets detailed in Section 5.1 on page 17 with existing published results. In Section 4.2 on page 16 the weighted spherical harmonic code is verified by adding equal weights to the data set used for the unweighted data to ensure the produced field has the same pattern, and that adding a lot of weight to one point distorts the field towards that point

4.1. Test results for an unweighted spherical harmonic field

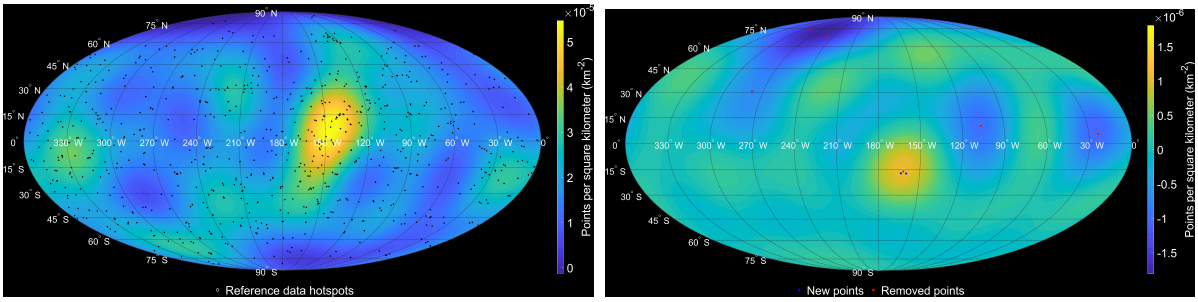

(a) Reference data. *(b) Difference with van Sliedregt (2020).*

Figure 4.1: A comparison of the spherical harmonic field for Reference data and for the data from van Sliedregt (2020) at harmonic degree 6. The Reference data is the same as the data from van Sliedregt (2020), except that the Reference data is updated using the Io GIS database from Williams et al. (2021). Subfigure (a) shows the spherical harmonic field at degree l = 6 for the Reference data, and subfigure (b) shows the difference between the spherical harmonic field of the Reference data shown in (a) and Figure 2.9 from van Sliedregt (2020). The colorbars are different so the patterns in the field are clearly visible for both subfigures. The anti-Jovian point is in the center of the images at 180 °W.

One of the data sets described in Section 5.1 on page 17 will be used for testing the unweighted spherical harmonic expansion, because that data set is nearly identical to one used in the Thesis by van Sliedregt (2020). This data set is called the Reference data. The main difference, as also detailed in Section 5.1 on page 17, is that data obtained from Veeder et al. (2015) used to construct the Reference data has been updated using the Io GIS database (Williams et al., 2021). The difference between van Sliedregt's data set and the Reference data is the removal of 6 points and the addition of 2 new ones. Figure 4.1 shows the spherical harmonic field at harmonic degree l = 6; Figure 4.1a is created using the Reference data set from this Thesis, and the difference between this field and the field in Figure 2.9 (also degree 6) from van Sliedregt (2020) is shown in Figure 4.1b. A visual comparison between Figure 2.9 from van Sliedregt and Figure 4.1a shows they are very similar, and indeed Figure 4.1b shows that the only differences are at the locations that are different between the Reference and the

data set used by van Sliedregt. The difference in magnitude of the signal in both subfigures highlights why the difference between Figure 4.1a and Figure 2.9 from van Sliedregt is near impossible to spot by eye, but also nicely confirms that the code used to generate the spherical harmonic expansion, and by extension these figures, is working correctly.

4.2. Test results for a weighted spherical harmonic field

In this subsection the correctness of the code calculating the spherical harmonic expansion with weights is checked. This is done using two tests. For the first test artificial weights are added to the Reference data, these weights are the same for all points. The second test involves adding more weight to a singular point. For the first test, weights of 1 are chosen for convenience. The resulting field should be identical to the unweighted data set at each degree with the way the weighted field is calculated. For the second test, adding more weight to only a single point should result in the spherical harmonic field centering around that point at high enough weights.

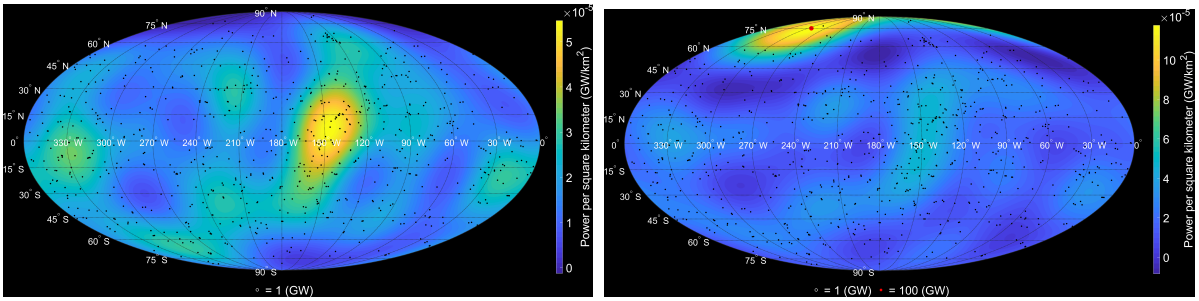

(a) Uniform weights of 1 (GW).

(b) One weight is 100 (GW) instead of 1 (GW).

Figure 4.2: The weighted spherical harmonic calculations are tested by adding uniform weights to an existing data set analyzed using spherical harmonics, as seen in subfigure (a). This has the same shape as Figure 4.1a for the unweighted spherical harmonic field, so is accurate. Subfigure (b) shows the second test, where a single point with higher weight should distort power in the existing field towards itself. The colorbar for (b) is different from (a) to highlight the loss of detail for the rest of the field in subfigure (b). Both fields are for harmonic order l = 6. The black dots are the hotspot locations for the Reference data. The anti-Jovian point is in the center of the images.

The results for the first test can be seen in Figure 4.2a. Clearly this is the same field with the same values as Figure 4.1a. The units are different between both field, because the assigned power is set to be 1 (GW). The weights could, of course, be unitless, resulting in the weighted and unweighted field having the same unit, but only power is used for weights in the rest of this Thesis, so that is also used here.

The results for the second test are shown in Figure 4.2b. Here, a single point has been given a weight of 100 (GW). This number is set to be large relative to the total weight of all points, so that a significant effect may be observed in the spherical harmonic field. For example, a weight of 2 (GW) compared to the total power would not have made noticeable difference as that point contains only $2/791 \cdot 100\% = 0.25\%$ of the total power; using a 100 (GW) means this point contains $100/890 \cdot 100\% = 11\%$ of the total power. In Figure 4.2b the impact of this weight is very apparent, because most power is now concentrated at the heavily weighted point close to the North pole instead of near the equator. Seeing as adding uniform weights of 1 (GW) produced the same result as the unweighted data (barring a unit change) and adding more weight to a point shifts the signal to that point, Figure 4.2 indicates that the weighted spherical harmonic expansion including weights is functioning as intended.

5

Applying (weighted) spherical harmonics to Io's hotspot observations

In this chapter the equations from Chapter 3 are applied to Io's hotspot distribution, and the results for the spherical harmonic expansion with and without weights are compared to the existing end-member models of Io's interior, which were discussed in Section 2.2 on page 4. Section 5.1 describes the data sets used to generate the spherical harmonic fields. Section 5.2 on page 21 goes into detail about how the optimal maximum harmonic degree for study is selected. Section 5.3 on page 25 shows the results of the spherical harmonic expansion for the hotspot distribution, split into the spherical harmonic field and the distribution of points along the latitude and longitude. Section 5.4 on page 27 is similar to Section 5.3, but for the spherical harmonic expansion for the hotspot distribution including the hotspot intensities. Section 5.5 on page 29 compares the weighted and unweighted results with each other. Section 5.6 on page 30 highlights the similarities between the Veeder2015 and Davies2024 data sets. Section 5.7 on page 31 goes into detail about how the result of the spectral power for the weighted data compares to the spectral power of the unweighted data and what the impact is on the model outputs of the weighted spherical harmonic expansion.

5.1. Selection of data sets

This Thesis is a continuation of a specific part of van Sliedregt's Thesis (van Sliedregt, 2020), namely the spherical harmonic analysis. To that end, this section will recap the data sets used by Sliedregt, how they were processed, how they are used for this Thesis, as well as what new data is used here.

It would be ideal to have a single data set containing all hotspots on Io, however the different instruments used for observing Io mean that observations of a hotspot from one instrument may of may not overlap with another due to measuring different qualities and measuring them at different times. Alternatively, observations of one hotspot may have overlap with a different relatively close by hotspot. Additionally, the post-processing of obtained data can be done in different ways depending on what exactly one is looking for, which in turn can lead to differences in the final results between different works. As a result of this there exist many different data sets with differing amount of hotspots. For example, one work may focus specifically on dark patera (Veeder et al., 2011) (i.e. current or recently active hotspots that are warm enough to prevent sulfurous compounds from settling on top of them), while another using different instruments looks at thermal emissions in the infrared (de Kleer et al., 2019b); these data sets are bound to have some overlap. To combine data sets to create a larger data set, it is necessary to filter out overlapping data points, to avoid a single hotspot being represented twice. This leads to the creation of a combined data set that filters out duplicate hotspots referred to in this Thesis as the 'Reference' data.

Unfortunately, not all data subsets that compose the Reference data include the hotspot intensity, so in order to be able to use that an additional data set is needed. That is where the paper from Davies et al. (2024) comes in, because this contains 343 hotspots and intensity data is available for all of them. Data from this article is referred to as the 'Davies2024' data set, which can be used both with and without intensities to compare it with the Reference data. There is one data set used to create the

Reference data that does have the intensity of each hotspot included, and that is the data from Veeder et al. (2015). However, because that is a precursor of the Davies2024 data, this data set is used only in support of the other two main data sets in this Thesis.

Of the two main data sets used in this Thesis, the Reference data is only used for the unweighted spherical harmonics, and the Davies2024 data is used for the weighted and unweighted spherical harmonics. To a lesser extent, a modified version of the Veeder2015 data is used as well. The three data sets just mentioned are treated in greater detail in their own subsection later on in this section.

Table 5.1: This is an overview of the data sets used for this Thesis. For each data set the instruments used to compile them have been marked.
Sources from the second column onward: Hamilton et al. (2013), the third column refers specifically to the N = 529 paterae data set from Hamilton et al. (2013), Veeder et al. (2015), de Kleer et al. (2019b) and Mura et al. (2020). After the second vertical line the two main data sets used in this Thesis are listed: the Reference data is combination of the five sources mentioned to its left, and the Davies2024 data is based on the information from Davies et al. (2024).

Carrier and Instrument	Hamilton Hotspots	Hamilton - Paterae	Veeder2015	deKleer	Mura	Reference data	Davies2024
Voyager – Imaging Science Subsystem (ISS)	X	X	X			X	
Voyager – InfraRed Interferometer Spectrometer (IRIS)			X			X	X
Galileo – PhotoPolarimeter-Radiometer (PPR)	X		X			X	X
Galileo – Solid State Imager (SSI)	X	X				X	X
Galileo – Near Infrared Mapping Spectrometer (NIMS)	X		X			X	X
Hubble Space Telescope – Near Infrared Camera and multi-Object Spectrometer (NICMOS)	X					X	
New Horizons – LOng Range Reconnaissance Imager (LORRI)	X					X	
New Horizons – Linear Etalon Infrared Spectral Array (LEISA)			X			X	X
Casini – ISS	X					X	X
Juno – Jovian InraRed Auroral Mapper (JIRAM)					X	X	X
Keck Observatory – Near-Infrared Camera, Second Generation (NIRC2) with Adaptive Optics (AO)	X		X	X		X	X
Gemini N Observatory – Near-InfraRed Imager (NIRI) with AO				X		X	X
Mauna Kea Observatory – National Aeronatics and Space Administration (NASA) InfraRed Telescope Facility (IRTF)			X			X	X

Table 5.1 gives an overview of the data sets relevant to this Thesis and the scientific instruments used to obtain the data; Section 2.1 on page 3 goes into more detail on the instruments. The data sets utilized by van Sliedregt are listed in columns 2 to 5 of this table, and the last two columns are unique to this Thesis. The Hamilton data set (Hamilton et al., 2013) is split into two, one contains the observed hotspots and the other the observed paterae. Hotspot data refers to locations of positive thermal anomalies while paterae are caldera-like depressions indicative of volcanic activity over longer timescales. The Veeder2015 data set (Veeder et al., 2015) has been updated for this Thesis to take into account new information on the intensity of several detections (Williams et al., 2021) that was not yet available at the time of van Sliedregt's Thesis. The de Kleer (de Kleer et al., 2019b) data set only has ground-based observations, and the Mura (Mura et al., 2020) data set focuses on data from Juno.

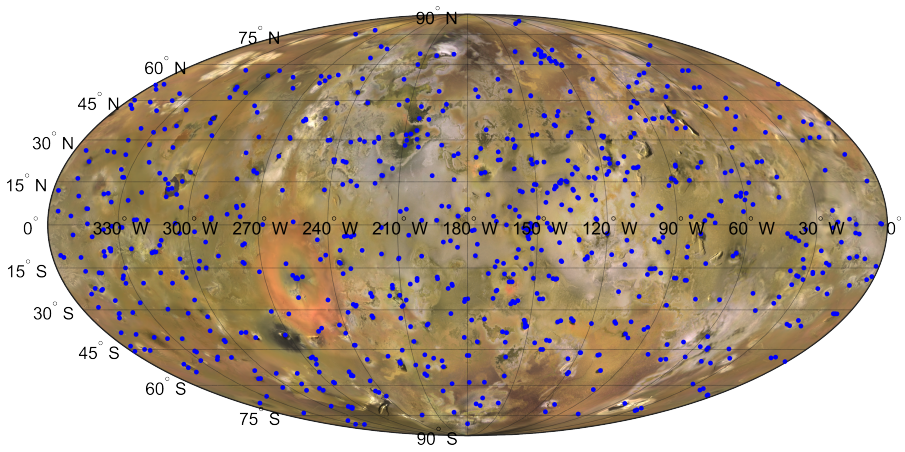

(a) Reference data set.

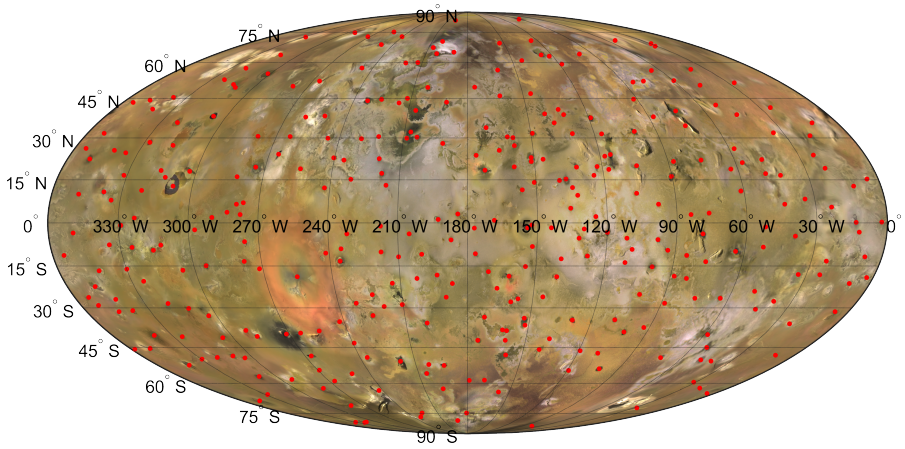

(b) Davies2024 data set.

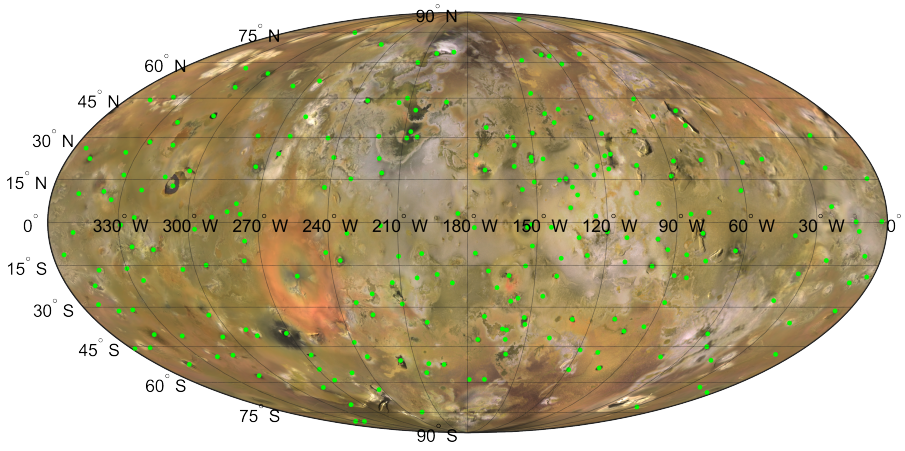

(c) Veeder2015 data set.

Figure 5.1: The locations of all volcanic centers for the three main data sets used in this Thesis. (a) shows the Reference data locations after filtering; see Table 5.1 on page 18 for the constituent data sets. (b) Shows all locations from the data set from (Davies et al., 2024). (c) shows all locations from (Veeder et al., 2015) excluding outburst eruptions. The color mosaic of Io is from Williams et al. (2011), and is created by combining Galileo SSI with Voyager ISS data.

5.1.1. Reference data

As mentioned earlier in this section the Reference data is not just a direct combination of all of the aforementioned data sets, because there would be a lot of identical, or close to identical, points. To avoid this, the constituent data sets are filtered according to the flowchart shown in Figure 5.2; this process is the same as the one used by van Sliedregt albeit with the Veeder2015 data set modified to include more up-to-date information available from the Io GIS database (Williams et al., 2021). Due to this update, the Reference data is slightly different from the final data set used by van Sliedregt. A comparison of the filtered data used by van Sliedregt and the Reference data from this Thesis can be found in Section 4.1 on page 15.

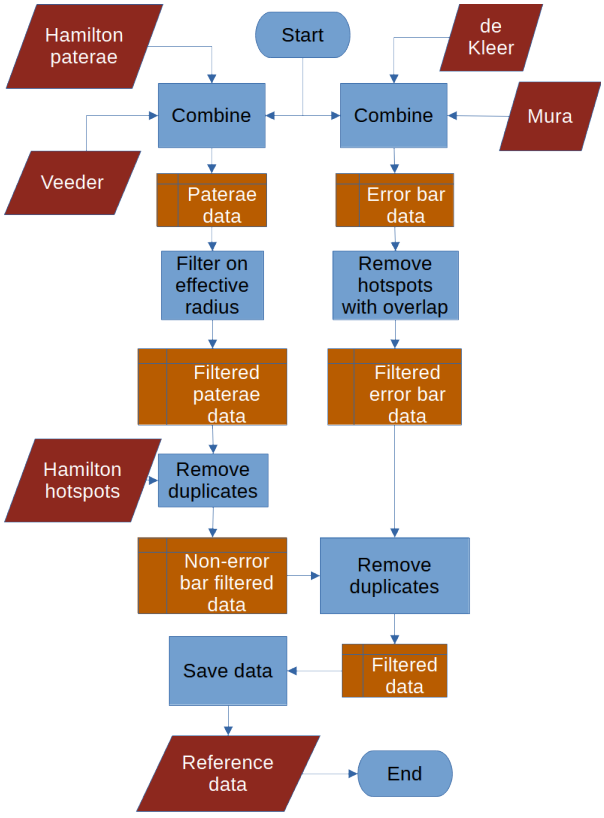

Figure 5.2: This chart shows the general process of creating the Reference data.

Figure 5.2 shows the general process used to create the Reference data; in this paragraph this process will be described in detail. For both the Hamilton Paterae data and the Veeder2015 data the effective radius is given for each point, so these data are compared with each other to check if they have overlapping hotspots, which are then removed (each hotspot has a corresponding area, which for simplicity is assumed to be circular during filtering). This is done by comparing the distance between two patera, and if it is smaller than both of their effective radii then it is assumed they refer to the same point and the point with the highest colatitude is removed. After this step the remaining points are filtered against the locations from the Hamilton Hotspots. The Hamilton Hotspots data is assumed to be perfectly accurate due to a lack of information on the uncertainty of their location, so if a Hamilton Hotspot is located within the effective radius of the previously filtered data, then the Hamilton Patera or Veeder hotspot is removed and the Hamilton hotspot is maintained. For the deKleer and Mura data the standard deviation in longitude and latitude is available for all points, so these sets are filtered against each other. The standard deviations are used to draw an ellipse around each point, and if the overlap from two ellipses at the 3σ confidence interval (a.k.a. there is a 99.7% chance that the estimation of a location is correct) contains both volcanic centers, then the point with the largest uncertainty is removed. Now one last process compares the results of the Hamilton Hotspot, Hamilton Paterae and Veeder2015 filtering processes with the remaining points from the deKleer and Mura data. If one of the

points from the Hamilton or Veeder sets is located within an ellipse from the deKleer and Mura data, then the deKleer/Mura point is removed. After the final step 690 hotspot locations are left, and these are shown in Figure 5.1a on page 19. The same procedure is used by van Sliedregt in his Thesis (van Sliedregt, 2020) and he finds 794 hotspots. This difference is solely due to changes to the Veeder2015 data set, because this data set is updated for this Thesis with the inclusion of new information from the Io GIS database (Williams et al., 2021). Using the information available to van Sliedregt at the time of his Thesis produces the same filtered data. Section 4.1 on page 15 demonstrates that the only difference between the Reference data from this Thesis and Duncan's data set is the six points that are different between the two.

5.1.2. Davies2024 data

The Davies2024 data set is fairly self-explanatory as it contains all 343 points mentioned in the article from Davies et al. (2024). This data set is used unmodified for both weighted and unweighted spherical harmonics, with one exception. Given Loki Patera's exceptional nature, with it being responsible for ± 10% of Io's total heat output (Veeder et al., 2012), a weighted spherical harmonic analysis of the Davies2024 data without Loki Patera is included in this chapter. The 343 locations of the complete Davies2024 data set are shows in Figure 5.1b on page 19.

5.1.3. Veeder2015 data

The Veeder2015 data set as a stand-alone data set, is different from how it is used in the Reference data. Of the Reference data constituents this is the only data set that has the intensity available for all points. As such this data is compared to the Davies2024 data in Section 5.6 on page 30. The Veeder2015 data is also used in Section 5.2 to help determine the most suitable harmonic degree to study. In order for the comparison with the Davies2024 to work, one change is made to this independent Veeder2015 data set, and that change is the removal of outburst detections. This reduces the amount of points in this data set from 250 to 242. The outburst detections have to be removed, because while they are incredibly powerful events they are also very transient compared the other hotspots, contributing only about 2% to Io's yearly heat flow budget (Davies, 2008). Whenever the Veeder2015 data set is mentioned in this and following chapters this data set without outbursts is meant, unless it is specifically mentioned to be the data used to create the Reference data. The 242 non-outburst locations are shown in Figure 5.1c on page 19.

5.2. Selecting the best harmonic degree for comparing the data

In this section the way the optimal harmonic degree is selected will be explained. See Chapter 3 starting on page 9 for the equations used to calculate the spherical harmonic field for each degree. For clarity, if a field is only referred to by its harmonic degree, then this refers the sum of all fields for all degrees (l) and orders (m) up to and including the mentioned harmonic degree.

The best fitting field, created be Equation (3.7) (and Equation (3.14) for the weighted spherical harmonics), is reached at an infinitely large degree and order. This isn't very practical, but given that the desired result from the spherical harmonic expansion is to find long wavelength signals, some upper limit can be placed on the number of degrees to examine. This is done by rewriting Equation (3.5) as $l = 2\pi R/\lambda_l$, so the degree l can be calculated for a given wavelength. This wavelength, as mentioned, has to be a long wavelength, otherwise it can't be directly related to global heat flow processes in the interior of Io. There isn't any existing limit defined for this, so a first approximation of this limit is taken to be the wavelength where it becomes smaller than the order of magnitude of the radius of Io. To connect numbers to this statement, the radius of Io R is 1821.6 (km), so any degree with a wavelength below 1000 (km) is assumed to have a wavelength too short to correspond to a signal related to global heat flow based processes. This comes out to be all degrees greater than $l = 11$ (as a first approximation). This choice for the upper limit will be examined further later in this section.

Now that an upper limit is established, all that remains is to determine which of the remaining harmonic degrees is the best one to use when looking for long-wavelength signals. One method that has been used before is to look at the spectral power for each degree as determined by Equation (3.8), see for example Kirchoff et al. (2011), which finds a statistically significant degree 2 signal in the distribution of volcanic centers. This strong degree 2 signal can also be found, albeit in a different way, in papers such as Veeder et al. (2012) where their model shows two maxima across Io's longitude. This strong

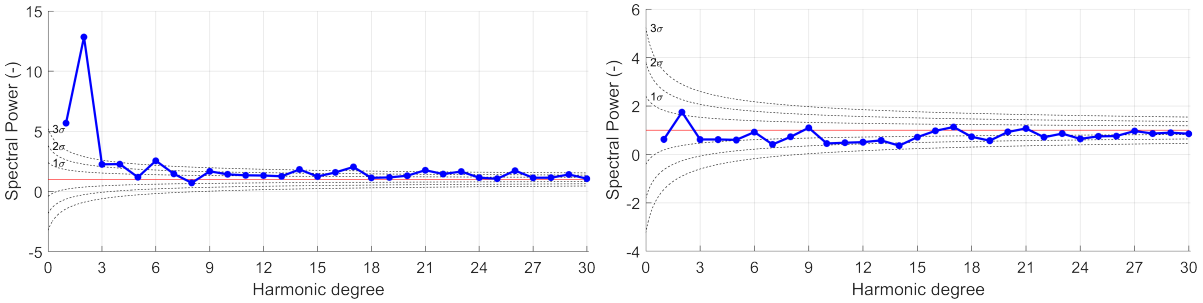

(a) Spectral power for the Reference data.

(b) Spectral power for the Davies2024 data.

Figure 5.3: Spectral power for the unweighted spherical harmonic expansion for the Reference and Davies2024 data sets. Up to degree 30 is shown to give an indication of the behavior at shorter wavelengths.

degree 2 signal is also found in the data sets used in this Thesis for the unweighted spherical harmonics when examining their spectral power. See Figure 5.3 for the spectral power of the distribution of volcanic centers for several harmonic degrees. Both the Reference data and the Davies2024 data show a peak at harmonic degree 2, although the peak for the Davies2024 could still be attributed to random chance. This prevalence of a degree 2 signal in existing literature means this is one of the harmonic degrees that will be studied further in this Thesis.

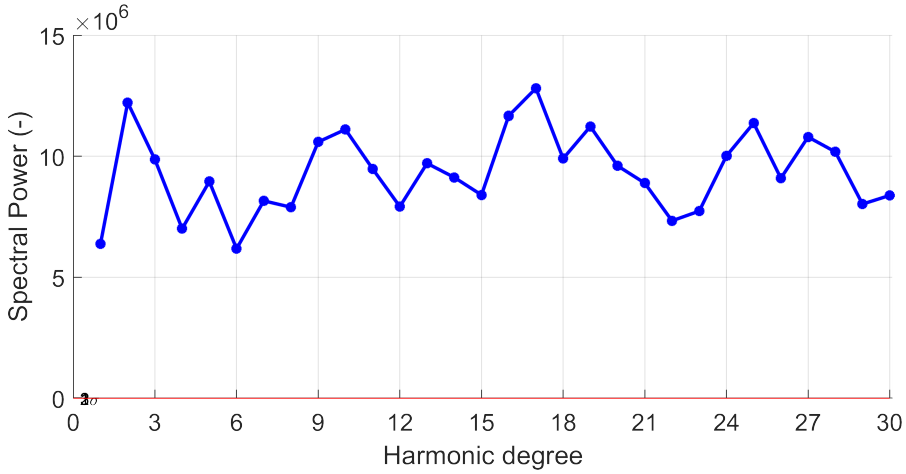

Figure 5.4: Spectral power of the weighted spherical harmonic expansion for the Davies2024 data. Up to degree 30 is shown to give an indication of the behavior at higher degrees.

Unfortunately, this method of selection does not hold up for the weighted data (the data with intensities per hotspot included). As can be seen in Figure 5.4 there is not a single clear peak at any degree, instead the normalized spectral power is high at all degrees. It is also far beyond the 3σ boundary (which is barely visible at the bottom-left). With such massive differences between the weighted and unweighted data for the spectral power, a different method of comparison will be used to find the optimal harmonic degree to avoid a potentially unfair comparison. Section 5.7 on page 31 goes into more detail on the implications of the shape of Figure 5.4.

As an alternative to using the spectral power to find the best harmonic degree, consider that the harmonic expansion produces fields that fit the given data for a certain amount of degrees of freedom (based on the harmonic degree l), so if this field could be more directly compared to the points used to generate it, then this can be used as an alternative quantitative measure of the spherical harmonic analysis' accuracy. The spherical harmonic expansion produces fields as a set of points defined by their latitude and longitude, so if one divides this field into bins along the latitude and longitude, and integrates the values in that bin then the result (if normalized) can be compared to a summation of all the observations (again, if normalized) for those same bins. The difference between the observations (summed per bin) and the model (integrated per bin) for a given harmonic degree is used as an indication of how well the model fits with reality at that degree. This process is explained in more detail

below.

For the observations:

1. Divide the latitude/longitude into 30° bins (6 for latitude, 12 for longitude).
   A size of 30° is chosen to ensure bins don't end up empty and to allow a direct comparison with the articles by Davies and Veeder (e.g. Davies et al. (2024)).
2. Add all hotspots to the appropriate bin for both the latitude and the longitude.
   The result is that each bin contains the total number of hotspots contained within those 30°.
3. Normalize the number of hotspots per bin by dividing each bin by the total number of hotspots.
   Each bin now contains the fraction of the total number of hotspots.

For the spherical harmonic expansion (the model) at harmonic degree l:

1. Divide the latitude/longitude into 30° bins.
2. The spherical harmonic field is defined to have 1 point at each degree, so to 'sort' this into bins it is necessary to integrate the field between the relevant latitudes and longitudes. For example, the latitude bin from -60 °N to -30 °N contains all field values from -60 to -30 °N across all longitudes; and the longitude bin from 240 °W to 270 °W contains all field values from 240 to 270 °W across all latitudes.
   (a) However, this does not take into account the varying area of the bins. Each point of the field represents a 1° x 1° area of the surface of Io, and this area changes when the latitude increases or decreases. So a correction factor has to be applied when integrating across multiple latitudes. This area-correction factor is calculated using Matlab's *areaquad* function; this function calculates the area on a sphere and so is perfectly suited for the task.
3. Normalize the density per bin by dividing each bin by the total field density, obtained by summing all bins, because that includes the latitude area-correction factor discussed in the subpoint above. Each bin now contains the fraction of the total field density.

Both the observation and model derived parameter (values in the bins) are now unit-less and by subtracting them a quantitative difference between the model and the observations can be calculated. The sum of the absolute values of these differences across all latitudes or longitudes indicates how well the model at harmonic degree l fits the observations for the latitude or longitude, respectively. Some loss of information due to compressing the spherical harmonic field into a single point per bin is inevitable, but this does allow an alternative quantitative comparison between the models generated by the spherical harmonic expansion and the observations, instead of the spectral power. By performing the above calculations across all harmonic degrees of interest one can compare these results and find the degree that has the smallest difference and is therefore the best fit to the data. In our case this range of interest is from degree 0 to 11, though higher degrees up to l = 30 will be included to check the behavior of spectral power at higher degrees and whether l = 11 can be kept as a permanent upper limit.

For the weighted spherical harmonics the process is identical, except for the observations the emitted power per bin is calculated instead of the number of hotspots, and for the spherical harmonic model the power density is calculated instead of the point density (the process is the same).

Figure 5.5 on page 24 shows an example of the final result for the Davies2024 data, where Figure 5.5a shows the differences between the observed data and the model for the unweighted data (without hotspot intensity), and Figure 5.5b shows the differences between the observed data and the model for the weighted data (including hotspot intensity). One can see the latitude and longitude differences start stabilizing at higher harmonic degrees, with the latitude differences stabilizing especially quickly. Evaluating the choice of l = 11 as an upper limit, Figure 5.5 (which is representative of the other data sets used in this section) shows that the difference between consecutive harmonic degrees is small at this point when checking the latitude distributions. The longitude distributions still shows the occasional stronger change, but the higher harmonic degrees directly after 11 show fairly little change. As will be discussed in Section 5.4, the weighted data, which shows larger changes for higher degrees, focuses around Loki Patera at degrees starting as low as (arguably) 2 and 4, with the signal focusing more and more around that point at even higher degrees. This means that going to degrees even higher than 11

will not show new information. So as an upper limit for the degrees of interest l = 11 is a reasonable choice.

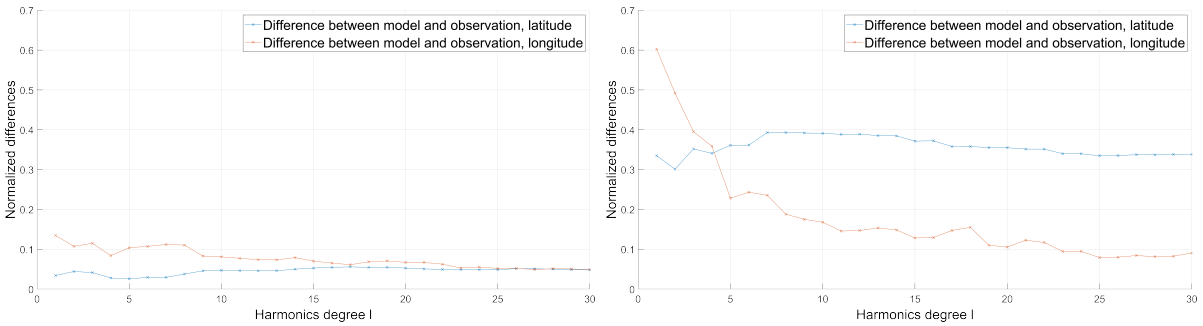

(a) Hotspot count and density.

(b) Hotspot power and power density.

Figure 5.5: Difference as described in the main text between the input data (observations) and the model (spherical harmonic field), for both the latitude and longitude, for each harmonic degree, for the Davies2024 data. Degrees up to l = 30 are included to show behavior at higher degrees. (a) shows the difference for the unweighted spherical harmonic expansion, so only based on the location of the hotspots. (b) shows the difference for the weighted spherical harmonic expansion, so based in the intensity distribution of the hotspots.

The best harmonic degree, without further constraints, would be at an infinitely large degree, as that results in the perfect fit to the data. A tentative upper limit of l = 11 has been established for low degrees. However, because the fit between the model and observations gets better with higher degrees (generally speaking, local increases may occur), this may result in 11 becoming the best fit for several cases. For example, in Figure 5.5 one can see that the best fit is at l = 11 for the longitude difference for the hotspot count/density (5.5a) and the hotspot power/power density (5.5b), when taking into account the upper limit of 11. To avoid this, instead, the best local minimum difference no larger than l = 11 is used, because for a small range of degrees this local minimum is the best fit, and it avoids the minimum moving towards higher degrees. As mentioned earlier, higher degrees do not produce new information, so those are to be avoided. These best local minima are calculated for the Reference data, Davies2024 and Veeder2015 without weights; and for the Davies2024 data, Davies2024 data excl. Loki Patera and the Veeder2015 data with weights. The result, for each data set, is shown in Table 5.2.

Table 5.2: An overview of the harmonic degree with the smallest differences between the input data and the field generated by the harmonic expansion.

Data set	Best local minimum, latitude	Best local minimum, longitude
Reference data	4	4
Davies2024, unweighted	5	4
Veeder2015, unweighted	4	5
Davies2024, weighted	2	5
Davies2024 excl. Loki Patera, weighted	4	6
Veeder2015, weighted	2	5

Table 5.2 is used to find the best harmonic degree for the latitude and longitude. For the unweighted data, regardless of the data set being considered, the best degree for both the latitude and longitude is at harmonic degree 4 or 5. For the weighted data sets the best local minimum is at degree 2 for the Davies2024 and Veeder2015 data, in fact they have the same minima for both longitude and latitude. This isn't entirely unexpected seeing as the Davies2024 data set is built on the Veeder2015 data, with corrections and more recent detections. The Davies2024 data without Loki Patera has the best local minimum at harmonic degree 4, which for the complete Davies2024 is a weak local minimum, and is completely absent as a minimum in the Veeder2015 data. The harmonic degree 2 has already been selected a degree of interest at the beginning of this section, because of this and the prevalence of degree 4 as the best local minimum for the latitude, harmonic degree 4 is selected the best option for the latitude. For the longitude the most prevalent local minimum is at degree 5, but this is very close to degree 4 and because having the same degree for both latitude and longitude is convenient, harmonic

degree 4 is selected as the best option for the longitude as well as the latitude.

5.3. Spherical harmonics applied to hotspot locations

In this section the result of applying the spherical harmonic expansion, as discussed in Section 3.1 on page 9, to Io's hotspot distribution is shown. These results will also be compared to existing interior models of Io mentioned in Section 2.2 on page 4. Recall that the deep mantle model results in high emitted power at the poles and low power at the sub- and- anti-Jovian points, the asthenospheric heating and magma ocean model have low heat emitted at the poles and more at the equator, the asthenospheric model has the highest heat flow offset slightly to the north and south of the sub- and- anti-Jovian points, and the magma ocean has the highest heat flow offset along the equator away from the sub- and- anti-Jovian points. Subsection 5.3.1 contains the spherical harmonic fields produced using the hotspot distribution. Subsection 5.3.2 on page 26 highlights the latitudinal and longitudinal distribution of the number of points, and the point density derived from the spherical harmonic fields.

5.3.1. The spherical harmonic fields of the hotspot locations

The two data sets used in this section are the Reference data, which is a filtered data set composed from various sources, and the Davies2024 data. For a more detailed explanation of these data sets, including their sources refer to Section 5.1 on page 17.

The results of the spherical harmonic expansion will be shown for harmonic degree 2 and 4. Degree 2 is chosen, because that is the one most relevant for existing papers discussing the hotspot distribution (e.g. Kirchoff et al. (2011) and Veeder et al. (2012)). Degree 4 is selected based on the selection prodecure detailed in Section 5.2 on page 21. Figure 5.6 shows the resultant spherical harmonic fields for the above mentioned harmonic degrees.

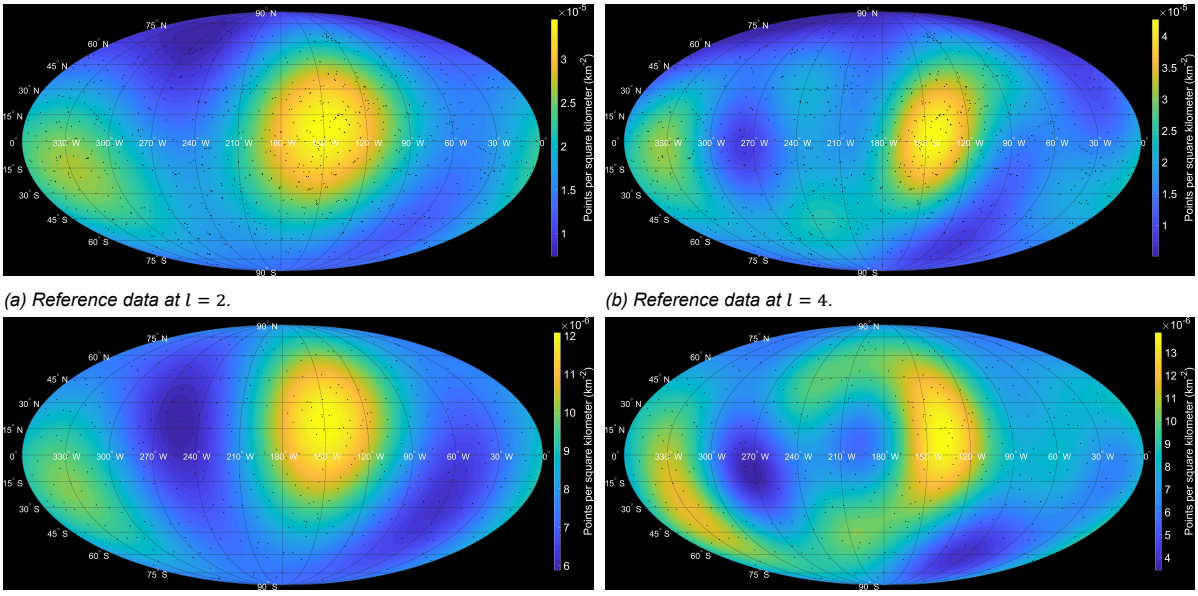

(a) Reference data at $l = 2$.

(b) Reference data at $l = 4$.

(c) Davies2024 data at $l = 2$.

(d) Davies2024 data at $l = 4$.

Figure 5.6: The spherical harmonic field at harmonic degree 2 and 4 for the Reference and Davies2024 hotspot distributions. The black dots are the hotspot locations. The colorbars are different for each subfigure to preserve the maximum amount of detail for each field. The colorbars between (a) and (c), and (b) and (d) are of different magnitude, because the fields show the number of hotspots per square kilometer, and the Davies2024 contains fewer hotspots than the Reference data. The anti-Jovian point is in the center of the images at 180 °W.

Examining the spherical harmonic fields in Figure 5.6 one can see that the degree 2 fields are very similar for both data sets with two major concentrations of points close to the equator, although the point of highest density is noticeably shifted north in Figure 5.6c. The degree 4 fields show more locations of relatively high density, which is possible thanks to the increase in degrees of freedom, but the point of highest density still coincides with the highest density at harmonic degree 2. The high density at approximately 15 °S and 300 °W is present in some form in all subfigures, except Figure 5.6d where it

is stretched across more latitudes on the southern hemisphere.

Comparing the modeled data shown in Figure 5.6 with existing end-member models summarized in Table 2.1 on page 6 and shown in Figure 2.3 on page 7, the results show no real similarity to the Deep Mantle heating model and more with the asthenospheric heating model, due to the points of higher density being located slightly to the north and south of the equator at the anti-Jovian point, and some similarity to the Magma Ocean heating model arises from the offset to east of the sub- and- anti-Jovian point for the locations of highest density.

5.3.2. The latitudinal and longitudinal locations of the hotspots

To visualize how well the fields generated by the spherical harmonic expansion fit to the hotspot observations, the latitude and longitude are divided into 30° bins for latitude and longitude and all points falling in each bin are added to each other for the data sets, and for the spherical harmonic fields at degrees 2 and 4. The spherical harmonic field is composed of 181 x 360 points, 181 points for the (co)latitude because both poles are included and don't repeat like the longitudes. By using a separate y-axis for the number of hotspots per bin and the density per bin an easy visual comparison can be made. Note that a more direct comparison involving normalizing both these data sets is described in Section 5.2 on page 21, but is not used further here, because that section already lists the best fits up to harmonic degree 11 in Table 5.2 on page 24. The figures in this and following sections are purely for qualitative reference, and to determine the locations of high number of points and density.

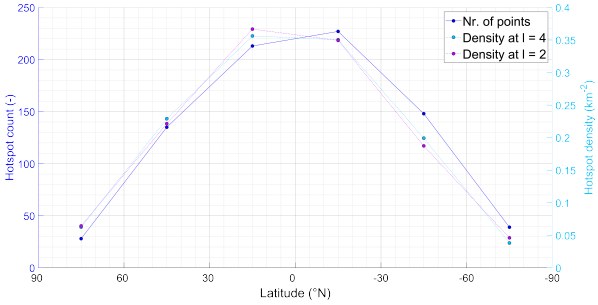

(a) Latitudinal distribution of the Reference data.

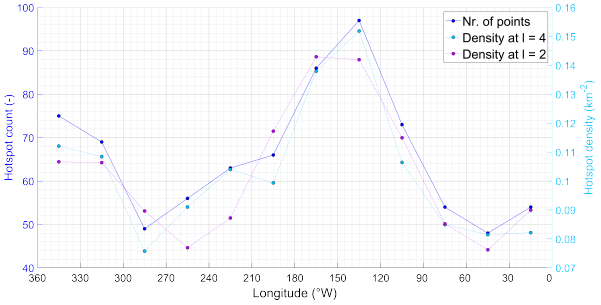

(b) Longitudinal distribution of the Reference data.

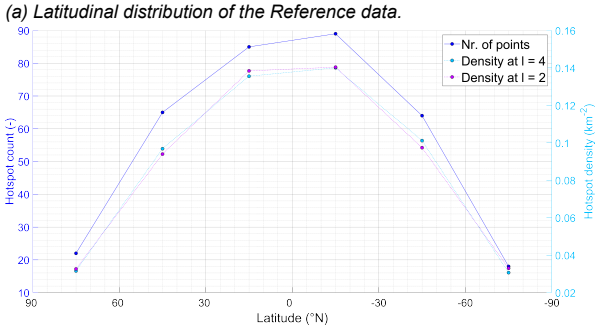

(c) Latitudinal distribution of the Davies2024 data.

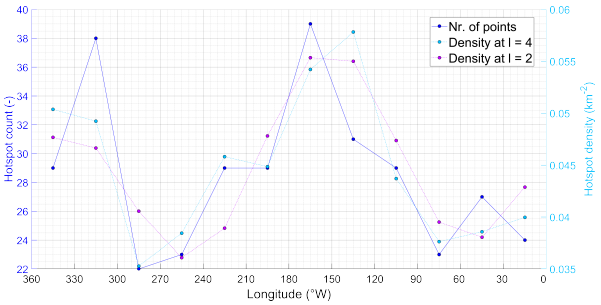

(d) Longitudinal distribution of the Davies2024 data.

Figure 5.7: This figure shows the hotspot count across latitude and longitude for the Reference and Davies2024 data sets, and the density distribution (calculated by integrating the spherical harmonic field over each bin) is shown for harmonic degrees 2 and 4.

Examining Figure 5.7 one can see that the point density is very similar to the number of points for the same latitude and longitude in subfigures 5.7a, 5.7b and 5.7c, with the best fit being degree 4 (as is to be expected given the results of Section 5.2). The density distribution also fits fairly well with the number of points per bin for subfigure 5.7d, though here there is a notable difference near the peak in the 315 °W bin which the spherical harmonic representation doesn't match very well. The highest concentration of points on a latitude basis is at the 15 °S bin, due to the highest and second highest density locations overlapping at that latitude (see also Figure 5.6). For the longitude the spherical harmonic expansion has trouble fitting the secondary maximum close to the sub-jovian point, but the primary maximum at approximately 135 °W is matched well by the model, although there is an offset of 30 degrees longitude for the longitude fit of the Davies2023 data. The longitude distribution of points for the Davies2024 in Figure 5.7d clearly shows the two locations of high density that have been noticed

before (e.g. Kirchoff et al. (2011)).

As far as a comparison to existing end-member models is concerned, using Table 2.1 and Figure 2.3 in Section 2.2, the latitude density points to the Asthenospheric heating and Magma Ocean heating models. The longitude density points more towards the shifted maxima seen in the Magma Ocean heating model. This is similar to what is seen in Figure 5.6, which is expected as the figures in this section are derived from the spherical harmonic field for the density distribution.

5.4. Spherical harmonics applied to hotspot intensities

In this section the result of applying the weighted spherical harmonic expansion, as discussed in Section 3.2 on page 11, to the hotspot intensity distribution is shown. These results will also be compared to existing interior models of Io. Subsection 5.4.1 contains the spherical harmonic fields produced using the hotspot intensity distribution. Subsection 5.4.2 on page 28 highlights the latitudinal and longitudinal distribution of the hotspot intensity, and the power density derived from the spherical harmonic fields.

5.4.1. The spherical harmonic fields of the hotspot intensities

The data set used in this section is the Davies2024 data, and a variation thereoff that excludes Loki Patera. The Davies2024 is examined without Loki Patera to determine the impact of removing the strongest hotspot. This does not mean Loki Patera can be ignored in any way, because it is still responsible for ± 20% of all volcanic heat flow on Io (Veeder et al., 2012). For more details on the data sets, including their sources refer to Section 5.1 on page 17.

The results of the weighted spherical harmonic expansion will be shown for harmonic degree 4, as determined in Section 5.2 on page 21. The results will also be shown for degree 2, as that is the one that is the most relevant for existing papers discussing the hotspot distribution (e.g. Kirchoff et al. (2011) and Veeder et al. (2012)). Figure 5.8 shows the weighted spherical harmonic fields for the above mentioned harmonic degrees.

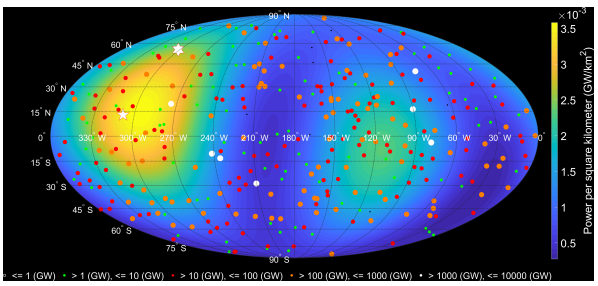

(a) Davies2024 data at $l = 2$.

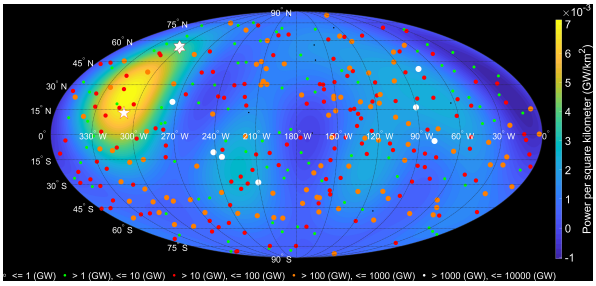

(b) Davies2024 data at $l = 4$.

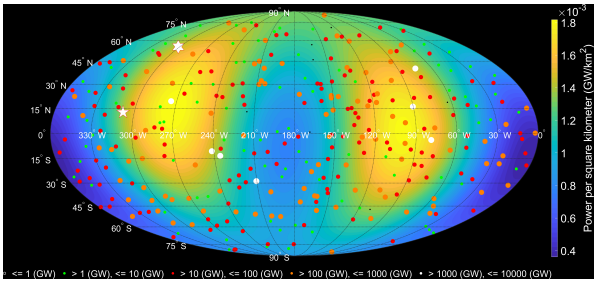

(c) Davies2024 data excluding Loki Patera at $l = 2$.

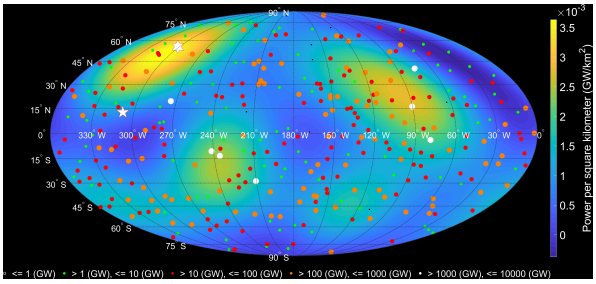

(d) Davies2024 data excluding Loki Patera at $l = 4$.

Figure 5.8: Shown here are the spherical harmonic field calculated using the weighted spherical harmonic expansion of the Davies2024 data, at harmonic degree 2 in subfigure (a) and harmonic degree 4 in subfigure (b); and the Davies2024 where Loki Patera has been removed, at harmonic degree 2 in subfigure (c) and harmonic degree 4 in subfigure (d). The colorbars are different for each subfigure to preserve the maximum amount of detail for each field. The points indicate location of each hotspot, and the color and size indicate the emitted power according to the legend shown at the bottom of each subfigure. In order of increasing power the color of the dots is black, green, red, orange and white. Loki Patera is shown as a white star with a red outline, and Dazhbog Patera is shown as a white hexagon with a red outline. The anti-Jovian point is in the center of the images.

Analysing Figure 5.8 it is clear by looking at Figure 5.8a and 5.8b that there is only one major concentration of power at approximately 15 °N and 300 °W, which is very close to Loki Patera. As Loki is

the strongest hotspot by a factor of 2, this makes sense. Subfigure 5.8a shows a weaker concentration close to the equator at roughly 120 °W, which is about where the primary density concentration was for the data excluding the intensity. While both the locations of hotspots and the power of hotspots are an indication of heat flow, the intensity is a more direct measurement, so this means that if one were to only look at locations one may misinterpret the location of highest heat flow.

The spherical harmonic field of the Davies2024 data shows significant differences with the Davies2024 data excl. Loki Patera. The highest concentration of power in Figure 5.8c moves about 30 degrees to the East of Loki Patera and the secondary maximum is now approximately the same strength as the primary one, compared to Figure 5.8a. Looking at degree 4 for the Davies2024 data excl. Loki Patera, Figure 5.8d reveals that the highest concentration of power without Loki Patera is now centered around Dazhbog Patera. Dazhbog Patera is the second most powerful hotspot on Io with a Power of ± 4 (TW), so a bit less than half of Loki Patera. The other smaller concentrations of power are also more noticeable than when Loki Patera was included, but in the same location as seen in Figure 5.8b. Comparing Figure 5.8b and 5.8d it's clear that the spherical harmonic expansion will quickly center around the most powerful hotspot when the difference in power (weights) is large, something that is also seen in the testing for weighted spherical harmonics in Figure 4.2 in Chapter 4.

Comparing the modeled data shown in Figure 5.8 with existing end-member models summarized in Table 2.1 on page 6 and shown in Figure 2.3 on page 7, the results show no strong correspondence to the Deep Mantle heating model, just like the spherical harmonic field generated for the hotspot locations excluding the intensity. The spherical harmonic field is significantly concentrated around Loki in most cases, so is fairly equatorial, pointing towards the Asthenospheric heating model. Due to Loki Patera's location the spherical harmonic expansion also points to the Magma Ocean model due to the offset from the anti-Jovian point. Excluding Loki, for harmonic degree 4, which is a better fit than degree 2, the power is distributed more uniformly across the planet instead of only being focused around Loki Patera. That is a good fit for the Magma Ocean model, albeit there is a much stronger offset from the sub- and anti-Jovian points than expected based on the end-member model (Figure 2.3). So like the hotspot distribution the intensity data points to either the Asthenospheric and Magma Ocean models.

5.4.2. The latitudinal and longitudinal distribution of the hotspot intensities

Similar to Section 5.3, to see how well the fields generated by the spherical harmonic expansion fit to the hotspot observations, a similar process is used. However, instead of adding the number of points between two latitude/longitude boundaries, the power of hotspots is used. Similarly, instead of the point density, the power density is used. The results can be seen in Figure 5.9 on page 29. The power-lines in subfigures 5.9c and 5.9d are a match for the power per latitude and longitude shown in Figure 5 and 6 of Davies et al. (2024), confirming the Davies2024 data has been properly implemented.

Figure 5.9 shows that the power and power density per bin follow a roughly similar pattern for the Davies2024 data. One major difference between the observed and modeled data is that the maximum power shown in Figure 5.9a is shifted 30 degrees to the South in the modeled data for both harmonic degree 2 and 4. This may be explained in part by the size of the bins that has been used, and smaller bins could move these peaks closer together. Although, the other subfigures in Figure 5.9 and 5.7 show better overlap, so that's unlikely to be the only reason. Looking at Figure 5.8a and 5.8b this offset is caused by the presence of other weaker concentrations of power around 15 °S latitude. Other than the above mentioned difference the power density for the latitude, as seen in Figure 5.9a and 5.9c, is similar to the power per bin at both degree 2 and 4, for both the Davies2024 data and the Davies2024 data excluding Loki Patera.

The power density, at degree 4, follows the power across all longitudes well in Figure 5.9b. The power density for degree 2 is not able to match the peak caused by the presence of Loki Patera, and other hotspots, at the 315 °W bin. The degree 4 power density distribution in Figure 5.9d noticeably deviates from the power per bin near the local maximum at 225 °W, which is likely due to the presence of the higher power density seen at that longitude in Figure 5.8d.

Comparing Figure 5.9 to existing end-member models (see Table 2.1 and 2.3 in Section 2.2) indicates that latitude-wise the heat flow is close to the equator when including Loki Patera, and when excluding Loki the heat flow is more evenly spread across the planet excluding the poles. This lack of power at the poles means that the Deep Mantle heating model is a poor match. Instead, this points to the Asthenospheric or Magma Ocean heating models. Examining the longitude, the power is distributed fairly evenly, but with some noticeable peaks at 115 °W and at 225 °W, and of course a large

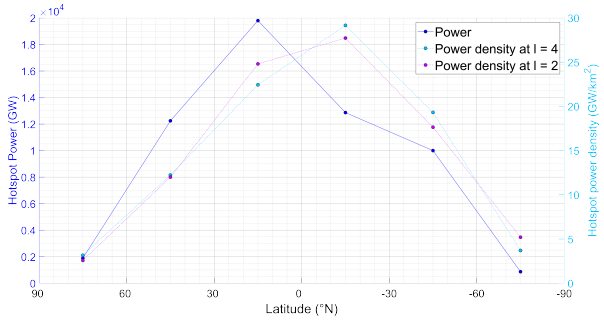

(a) Latitudinal distribution of the Davies2024 data.

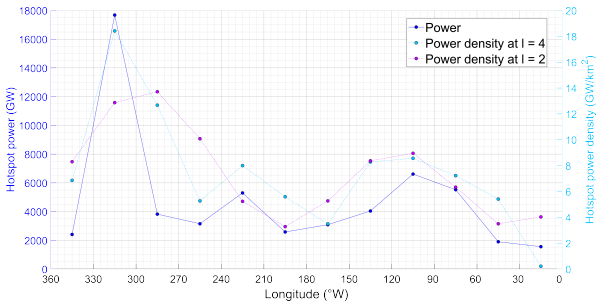

(b) Longitudinal distribution of the Davies2024 data.

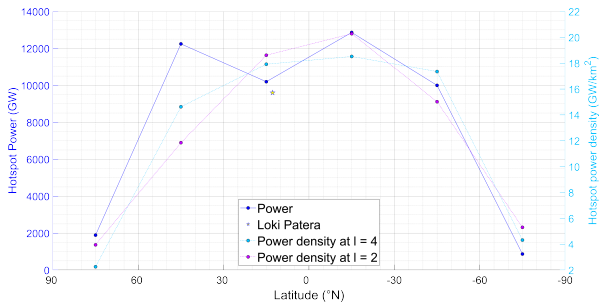

(c) Latitudinal distribution of the Davies2024 data excluding Loki Patera.

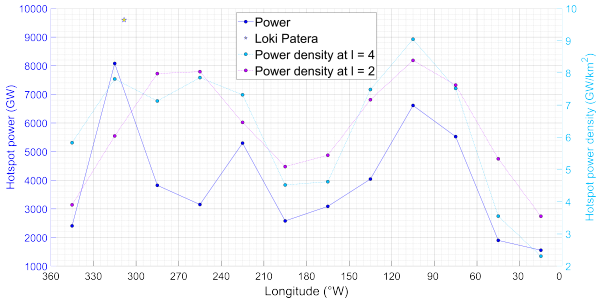

(d) Longitudinal distribution of the Davies2024 data excluding Loki Patera.

Figure 5.9: This figure shows the power across latitude and longitude for the Davies2024 data and the Davies2024 data without Loki Patera. The density distribution is shown for harmonic degrees 2 and 4. Note that the Power per bin (dark blue line) in subfigures 5.9c and 5.9d is exactly the same as the total power from Davies et al. (2024), in Figure 6 and 5 respectively.

peak at 315 °W due to most notably Loki Patera and Dazhbog Patera. So for the longitude the power distribution mostly corresponds with the Magma Ocean and Asthenospheric heating model.

5.5. Comparing the weighted and unweighted spherical harmonic expansions

From Section 5.3 on page 25 and Section 5.4 on page 27 it follows that regardless of whether the hotspot intensities are included in the spherical harmonics, the spherical harmonic expansion points towards the Asthenospheric heating or Magma Ocean heating end-member models (see Section 2.2 for details on said models). However, there are some notable differences and similarities between weighted and unweighted spherical harmonic expansions that need to be highlighted. This is done using the Davies2024 data set as it is complete with and without the hotspot intensities.

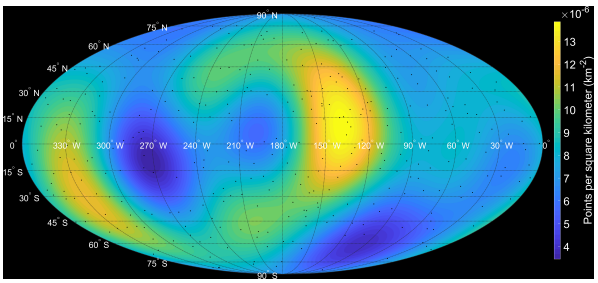

(a) Unweighted Davies2024 data.

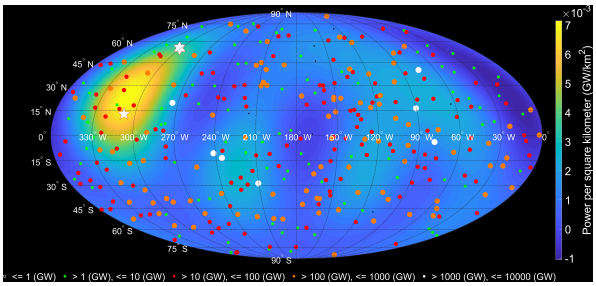

(b) Weighted Davies2024 data.

Figure 5.10: The spherical harmonic field at l = 4 for the Davies2024 data both with and without taking into account hotspot intensity. The colorbars are different, because they represent different quantities, km^{-2} for (a) and GW/km^2 for (b). The dots in both (a) and (b) represent the locations of the hotspots. The color of the dots in (b) indicates the emitted power according to the legend shown at the bottom of each subfigure. In order of increasing power the color of the dots is black, green, red, orange and white. Also (b) shows the location of Loki Patera as a white star with a red outline, and Dazhbog Patera as a white hexagon with a red outline. The anti-Jovian point is in the center of the images

Figure 5.10 shows the spherical harmonic field of the unweighted and weighted Davies2024 data next to each other for harmonic degree 4. Neither Figure 5.10a, nor 5.10b indicate strong polar heat flow from volcanic activity, so the Deep Mantle heating model is a poor fit for both. For both subfigures the heat flow is located more at the low and middle latitudes with a high (power) density close to the equator, indicating either the Asthenospheric heating or Magma Ocean heating model. However, this Figure also shows a flaw in using the volcanic location as the main indicator of heat flow. Looking at the point with the highest point/power density this is at about 135 °W for the unweighted data and at about 310 °W for the weighted data. Using the radiated power is a more direct indication of Io's heat flow than only the location of its hotspots, and that's shown very clearly in this figure, because the locations with the highest density of hotspots and the highest power density do not overlap. While it is possible that there are some unique local processes that result in Loki Patera being as outstanding as it is (see Section 2.3 on page 8), removing Loki Patera from the equation (see Figure 5.8d) still does not show the high density point seen at 135 °W in Figure 5.10a.

From Figure 5.10 it is clear that for both the weighted and unweighted Davies2024 data the locations of highest heat flow are not at the sub-Jovian or anti-Jovian point. Instead, they both have an offset to the east. This implies a more favorable fit with the Magma Ocean heating model than the Asthenospheric heating model. However, an upcoming article by Veenstra et al. (2024) demonstrates that in a model without a magma ocean, a feedback loop between tidal heating and melt generation also produces an eastward offset from the sub- and- anti-Jovian points for the highest concentration of heat. So both the Asthenospheric and Magma Ocean models remain a viable explanation for the spherical harmonic fields shown in Figure 5.10.

5.6. The similarities of the Veeder2015 and Davies2024 data

In Section 5.1 the Veeder2015 data is described, but other than the selection of the harmonic degree, it has not been used. The reason for this is that the corresponding spherical harmonic expansion is very similar to that of the Davies2024 data, see Figure 5.11. Their similarity isn't very surprising, seeing as the Davies2024 data contains corrections on and additions to the Veeder2015 data. Nonetheless, the Davies2024 data has an additional 101 points compared to the Veeder2015 data, so the fact the power densities are so similar shows that the most powerful hotspots are already included in the Veeder2015 data. This makes sense, because researchers have been trying to find unique hotspots on Io for several decades now (see Chapter 2). One notable difference between the Veeder2015 and Davies2024 is that the Davies2024 data has a better coverage of Io's poles (Davies et al., 2024), yet the power density has not changed all that much with respect to the total heat flow compared to the Veeder2015 data. If the Davies2024 data was changed so it only contained points already present in the Veeder2015 data, then perhaps it may be possible to make some observations about the change in emitted power over time. However, this is not the case. Figure 5.11 does show that the global heat flow can't have changed a lot in the years between these two data sets.

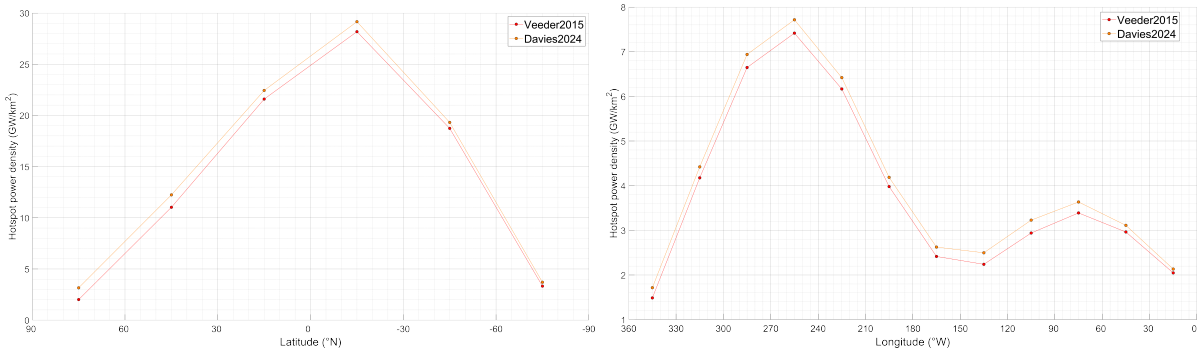

(a) Latitudinal power density. *(b) Longitudinal power density.*

Figure 5.11: Comparing the power density (calculated by integrating the weighted spherical harmonic field per bin) between the Veeder2015 data and the Davies2024 data, both only at harmonic degree 4.

5.7. On the spectral power for the weighted data

Comparing spectral power with and without the power of hotspots shows that for the weighted spherical harmonics there is no single or a few harmonic degrees with a high statistically significant spectral power. Instead all points have a high spectral power. The reason for this is in how the spherical harmonic expansion works and the fact that there is one hotspot that is much stronger than all the others, Loki Patera in this case. In essence, because of this single outstanding point, the spherical harmonic expansion can create a good fit around this one point at all harmonic degrees. For example, at degree 1 you can divide the moon into two parts (one positive, one negative) and Loki Patera can be made to fit this distribution; at degree 2 you divide the moon into three parts (positive, negative, positive; or alternatively negative, positive, negative) and Loki Patera can be made to fit this with little problem; this can be continued up to any harmonic degree and as a result a statistically significant fit can be made for all degrees and so they all have high spectral power. There is no degree that is a bad fit. As a result of this, while up to this point Loki Patera appears to be caused by long-wavelength processes, it is equally valid to pick a high harmonic degree and say that Loki Patera is a local phenomenon. See Section 2.3 on page 8 for current theories on whether Loki's origin lies deep in the planet or if it's closer to the surface. The spherical harmonic expansion is not wrong in either case, and the spectral power is high enough that both answers are equally valid. So while weighted spherical harmonics can highlight regions with high power density, on its own it cannot be used to determine whether this power has a local or global cause.

6

Conclusions and Recommendations

6.1. Conclusions

The main goal of this Thesis is to determine the viability of adding weights, representing hotspot intensity, to a spherical harmonic expansion of the hotspot distribution on Io, in order to find long-wavelength signals that could help clarify the interior processes of the innermost Galilean moon. The results of the weighted spherical harmonic expansion are used to exclude certain end-member models as representative of Io's heat flow, and this is compared to the results of the unweighted spherical harmonic expansion.

Given the need for long-wavelength signals only lower order harmonic degrees of the spherical harmonic expansion are relevant, because only those can come from Io's interior. Of those degrees, degrees 2 and 4 are selected as the best degrees to represent the used data sets. Harmonic degree 2 is selected due to its prevalence in existing literature such Kirchoff et al. (2011) and Steinke et al. (2020). This choice is supported by the spectral power calculations in this report, because for the unweighted spherical harmonic expansion there is a strong signal at harmonic degree 2. The selection of harmonic degree 4 is less straightforward, because the spectral power of the weighted spherical harmonic expansion doesn't have just one or two degrees with a strong signal, but instead has a high power at all degrees (this has been checked up to harmonic degree 30, which is well into the shorter wavelengths). So an alternative method to determine a strong fit between the model produced by the spherical harmonic expansion and existing observations is used. For the weighted and unweighted data the observations are divided into bins along the latitude and longitude, then the (weighted) spherical harmonic field is integrated for those same bins, while taking into account that areas represented by each point are different at different latitudes. After normalizing these results with the number of hotspots/power for the observations and the total of the binned field values for the model, the total magnitude of the difference between the observations and the model produced by the spherical harmonic expansion is used as an quantitative indication of how well the model fits the observations. Comparing this difference for lower harmonic degrees (to get a long wavelength signal) for several data sets, yields that harmonic degree 4 has the overall smallest difference between the model and observations for the studied data sets.

The high spectral power at all degrees for the weighted spherical harmonic expansion is caused by the nature of a spherical harmonic expansion and the large difference between the strongest hotspot and the second strongest. This leads to a concentration of power in a single point that can be fitted at all harmonic degrees. As a result, the weighted spectral power does not have one strong signal, but strong signals across all harmonic degrees. This spectral power distribution for the weighted spherical harmonic expansion means that one can look at a low degree, like 4, and argue that the main signal (Loki Patera) is caused due to long-wavelength related phenomena, which may originate from deep inside Io. On the other hand one can also choose a high degree and argue that the main signal is actually caused by a local phenomenon. Both arguments are valid when considering weighted spherical harmonics for Io, given the distribution of the weighted spectral power. So, unfortunately, adding the intensity to the spherical harmonic analysis cannot be used on its own to determine whether a detected signal is due to an interior process of Io. Existing literature also does not yet have a unified origin for

Loki Patera, with Loki being part of a strong degree 2 signal taken as indication for a global source (e.g. Veeder et al. (2009) and Veeder et al. (2011)), but Steinke et al. (2020) briefly mentions local rheology and ancient impacts can also explain Loki, and de Kleer et al. (2019a) mentions that the time-variability observed in Loki Patera's heat output could be due to geophysical factors.

The second goal of this Thesis is, as mentioned, to compare the best fitting end-member models for the weighted and unweighted spherical harmonic distributions. These end-member models are discussed in, for example, Pommier and McEwen (2022) and Lopes et al. (2023). The spherical harmonic distributions are compared at harmonic degree 2 and 4. Neither the weighted or unweighted spherical harmonic expansion show a match to Deep Mantle heating being the source of Io's volcanism, instead both indicate the Asthenospheric heating or Magma Ocean heating end-member models as being the best explanation for Io's volcanism. The weighted and unweighted spherical harmonic distribution do both show an eastward offset of the highest concentrations of emitted heat away from the sub-Jovian and anti-Jovian point in a way that favors the Magma Ocean model, but a soon to be published article by Veenstra et al. (2024) indicates this can also be explained by a feedback mechanism between melt generation and tidal heating without a magma ocean. An important distinction between the weighted and unweighted spherical harmonic analysis is that for the unweighted analysis the highest concentration of hotspots is at about 150 °W (30 °E of the anti-Jovian point) close to the equator and a secondary maximum at about 330 °W (30 °E of the sub-Jovian point) south of the equator, but for the weighted analysis the primary maximum is located at about 315 °W (45 °E of the sub-Jovian point) and just north of the equator and a secondary maximum at about 150 °W (30 °E of the anti-Jovian point) for degree 2 and no true secondary maximum for harmonic degree 4. This means that what appears to be the main location for heat outflow for the hotspot distribution, does not correspond directly to the hotspot(s) with the highest power output.

6.2. Recommendations

Some minor adjustments or improvements to the work presented in this Thesis are to investigate the impact of using a different bin size than 30°. A smaller binsize may lead to a better fit between the observations and the model created by the spherical harmonic expansion, using the method described in Section 5.2, though attention would have to be paid to ensure the bins don't become too empty with respect to the actual hotspot (power) observations.

The impact of a strong single point source, leading to high spectral power across all harmonic degrees for the weighted spherical harmonic expansion, may be mitigated somewhat by dividing a hotspot's power over its area. For hotspots the effective area (emitting area) is generally known, so if one assumes a circular hotspot as an approximation, one can then use this to divide the power that was located in a single point over multiple points equally divided over this area. Because the power of a hotspot tends to be distributed over a larger area instead of a single point, this may somewhat alleviate the problem of Loki Patera dominating all the other signals. However, even this larger area may still be too small compared to the total surface are of Io to have a significant impact.

Different types of volcano can have different underlying sources and behave differently over time. Investigating the time variability further between the Veeder2015 and Davies2024 could be a good start to reveal potential short term (geologically speaking) changes in volcanic activity on Io. One can do this by comparing the thermal output of specific hotspots available in both the Veeder2015 and Davies2024 data sets, and checking if it has changed over time and whether that change is due to new observations or differences in processing. This could be expanded to earlier observations, though the detected temperature would have to be converted to an emitted power, and not all hotspot data even has a corresponding temperature. Calculating the emitted power for different data sets that don't have it available, would increase the amount hotspots that can be used for studying time variability, but can also be used to update results from this Thesis.

Creating a distinction between different types of volcanic activity and performing the spherical harmonic analysis on each individual set of detections may help narrow down the activity taking place below Io's surface, because they may have a different source of be impacted differently by local variables such as volatile content in the magma or geology. One could, for example, divide the observations between lava lakes, outburst eruptions, patera with dark floors, bright or undivided floors, outflows, etc. A spherical harmonic analysis on these separated observations could support existing research on the distribution and intensity of specific types of hotspots (e.g. Veeder et al. (2009), Veeder et al. (2011)),

or create new insights when adding the respective power of each hotspot. For a lot of observations the emitted power does have to be calculated first.

One could also explore the relation between eruption type and the state of Io's orbit to try and narrow down the possible inner structure of Io, by checking to see which eruption properties are more directly linked to Io's tides. Similar studies have been performed by Kleer et al. (2019) and Rhoden and Kite (2011), and, outside of Loki Patera, have not found significant periodicities independent of observation timings. This could just be due to not having observed Io for long enough or frequently enough. So this option probably requires more observations before significant analysis can be performed.

Following from the previous recommendation, a dedicated satellite mission to Io capable of determining several physical parameters at once, such as the magnetic induction, surface temperature and gravity field variations would be incredibly useful to help constrain current models. Refer to Table 2.1 on page 2.1 for what results are expected for different end-member models.

Bibliography

J.D. Anderson, Tilman Spohn, and William Mckinnon. Interior composition, structure and dynamics of the Galilean satellites. pages 281–306. January 2004. ISBN 978-0-521-81808-7.

Aljona Blöcker, Joachim Saur, Lorenz Roth, and Darrell F. Strobel. MHD Modeling of the Plasma Interaction With Io's Asymmetric Atmosphere. *Journal of Geophysical Research: Space Physics*, 123(11):9286–9311, 2018. ISSN 2169-9402. doi: 10.1029/2018JA025747. URL https://onlinelibrary.wiley.com/doi/abs/10.1029/2018JA025747. _eprint: https://onlinelibrary.wiley.com/doi/pdf/10.1029/2018JA025747.

Iryna Chatila. Workshop: Tidal Heating – Lessons from Io and the Jovian System, 2024. URL http://kiss.caltech.edu/workshops/tidal_heating/tidal_heating.html.

Ashley Davies. Volcanism on Io: A Comparison With Earth. *Volcanism on Io: A Comparison with Earth, by Ashley Gerard Davies. ISBN-13 978-0-521-85003-2 (HB). Published by Cambridge University Press, Cambridge, UK, 2007.*, -1, January 2008. ISSN 9781107279902. doi: 10.1017/CBO9781107279902.

Ashley Davies, Jason Perry, David Williams, Glenn Veeder, and David Nelson. New Global Map of Io's Volcanic Thermal Emission and Discovery of Hemispherical Dichotomies. *The Planetary Science Journal*, 5:121, May 2024. doi: 10.3847/PSJ/ad4346.

Ashley Gerard Davies and Glenn J. Veeder. Near Infrared Spectral Radiance at Multiple Wavelengths From Io's Volcanoes 1: The Low Spatial Resolution Night-Time Galileo NIMS Data Set. *Journal of Geophysical Research: Planets*, 128(8):e2023JE007839, 2023. ISSN 2169-9100. doi: 10.1029/2023JE007839. URL https://onlinelibrary.wiley.com/doi/abs/10.1029/2023JE007839. _eprint: https://onlinelibrary.wiley.com/doi/pdf/10.1029/2023JE007839.

Ashley Gerard Davies, Glenn J. Veeder, Dennis L. Matson, and Torrence V. Johnson. Map of Io's volcanic heat flow. *Icarus*, 262:67–78, December 2015. ISSN 0019-1035. doi: 10.1016/j.icarus.2015.08.003. URL https://www.sciencedirect.com/science/article/pii/S0019103515003474.

Katherine de Kleer, Francis Nimmo, and Edwin Kite. Variability in Io's Volcanism on Timescales of Periodic Orbital Changes. *Geophysical Research Letters*, 46(12):6327–6332, 2019a. ISSN 1944-8007. doi: 10.1029/2019GL082691. URL https://onlinelibrary.wiley.com/doi/abs/10.1029/2019GL082691. _eprint: https://onlinelibrary.wiley.com/doi/pdf/10.1029/2019GL082691.

Katherine de Kleer, Ryan Park, and Alfred McEwen. Tidal heating: Lessons from Io and the Jovian System. Final Report, Keck Institute for Space Studies, June 2019b. URL http://kiss.caltech.edu/programs.html.

Christopher W. Hamilton, Ciarán D. Beggan, Susanne Still, Mikael Beuthe, Rosaly M. C. Lopes, David A. Williams, Jani Radebaugh, and William Wright. Spatial distribution of volcanoes on Io: Implications for tidal heating and magma ascent. *Earth and Planetary Science Letters*, 361:272–286, January 2013. ISSN 0012-821X. doi: 10.1016/j.epsl.2012.10.032. URL https://www.sciencedirect.com/science/article/pii/S0012821X12006012.

Krishan K. Khurana, Xianzhe Jia, Margaret G. Kivelson, Francis Nimmo, Gerald Schubert, and Christopher T. Russell. Evidence of a Global Magma Ocean in Io's Interior. *Science*, 332(6034):1186–1189, June 2011. doi: 10.1126/science.1201425. URL https://www.science.org/doi/10.1126/science.1201425. Publisher: American Association for the Advancement of Science.

Michelle R. Kirchoff, William B. McKinnon, and Paul M. Schenk. Global distribution of volcanic centers and mountains on Io: Control by asthenospheric heating and implications for mountain formation. *Earth and Planetary Science Letters*, 301(1):22–30, January 2011. ISSN 0012-821X. doi: 10.1016/j.epsl.2010.11.018. URL https://www.sciencedirect.com/science/article/pii/S0012821X10007132.

Katherine de Kleer, Imke de Pater, Edward M. Molter, Elizabeth Banks, Ashley Gerard Davies, Carlos Alvarez, Randy Campbell, Joel Aycock, John Pelletier, Terry Stickel, Glenn G. Kacprzak, Nikole M. Nielsen, Daniel Stern, and Joshua Tollefson. Io's Volcanic Activity from Time Domain Adaptive Optics Observations: 2013–2018. *The Astronomical Journal*, 158(1):29, June 2019. ISSN 1538-3881. doi: 10.3847/1538-3881/ab2380. URL https://dx.doi.org/10.3847/1538-3881/ab2380. Publisher: The American Astronomical Society.

Rosaly M. C. Lopes, Katherine De Kleer, and James Tuttle Keane, editors. *Io: A New View of Jupiter's Moon*, volume 468 of *Astrophysics and Space Science Library*. Springer International Publishing, Cham, 2023. ISBN 978-3-031-25669-1 978-3-031-25670-7. doi: 10.1007/978-3-031-25670-7. URL https://link.springer.com/10.1007/978-3-031-25670-7.

A. Mura, A. Adriani, F. Tosi, R. M. C. Lopes, G. Sindoni, G. Filacchione, D. A. Williams, A. G. Davies, C. Plainaki, S. Bolton, F. Altieri, A. Cicchetti, D. Grassi, A. Migliorini, M. L. Moriconi, R. Noschese, A. Olivieri, G. Piccioni, and R. Sordini. Infrared observations of Io from Juno. *Icarus*, 341:113607, May 2020. ISSN 0019-1035. doi: 10.1016/j.icarus.2019.113607. URL https://www.sciencedirect.com/science/article/pii/S0019103519304427.

NASA. https://science.nasa.gov/wp-content/uploads/2023/09/galileo.pdf?emrc=66bf9854b3cea, February 2009. URL https://science.nasa.gov/wp-content/uploads/2023/09/galileo.pdf?emrc=66bf9854b3cea.

NASA and JPL-Caltech. Galileo Fact Sheet - NASA Science, April 2023. URL https://science.nasa.gov/resource/galileo-fact-sheet/.

Imke Pater, Katherine Kleer, and Máté Ádámkovics. High Spatial and Spectral Resolution Observations of the Forbidden 1.707 μ m Rovibronic SO Emissions on Io: Evidence for Widespread Stealth Volcanism. *The Planetary Science Journal*, 1:29, July 2020. doi: 10.3847/PSJ/ab9eb1.

Imke de Pater, James T. Keane, Katherine de Kleer, and Ashley Gerard Davies. A 2020 Observational Perspective of Io. *Annual Review of Earth and Planetary Sciences*, 49 (Volume 49, 2021):643–678, May 2021. ISSN 0084-6597, 1545-4495. doi: 10.1146/annurev-earth-082420-095244. URL https://www.annualreviews.org/content/journals/10.1146/annurev-earth-082420-095244. Publisher: Annual Reviews.

Stanton Peale, P Cassen, and R Reynolds. Melting of Io by Tidal Dissipation. *Science (New York, N.Y.)*, 203:892–4, April 1979. doi: 10.1126/science.203.4383.892.

Thanh-Son Phạm and Hrvoje Tkalčić. Up-to-fivefold reverberating waves through the Earth's center and distinctly anisotropic innermost inner core. *Nature Communications*, 14(1):754, February 2023. ISSN 2041-1723. doi: 10.1038/s41467-023-36074-2. URL https://www.nature.com/articles/s41467-023-36074-2. Publisher: Nature Publishing Group.

Anne Pommier and Alfred McEwen. Io: A Unique World in our Solar System. *Elements*, 18:368–373, December 2022. doi: 10.2138/gselements.18.6.368.

Jani Radebaugh, Laszlo P. Keszthelyi, Alfred S. McEwen, Elizabeth P. Turtle, Windy Jaeger, and Moses Milazzo. Paterae on Io: A new type of volcanic caldera? *Journal of Geophysical Research: Planets*, 106(E12):33005–33020, 2001. ISSN 2156-2202. doi: 10.1029/2000JE001406. URL https://onlinelibrary.wiley.com/doi/abs/10.1029/2000JE001406. _eprint: https://onlinelibrary.wiley.com/doi/pdf/10.1029/2000JE001406.

A. Rhoden and Edwin Kite. Tidally-controlled volcanism at Loki Patera, Io? October 2011.

Nico Sneeuw. Global spherical harmonic analysis by least-squares and numerical quadrature methods in historical perspective. *Geophysical Journal International*, 118(3):707–716, 1994. ISSN 1365-246X. doi: 10.1111/j.1365-246X.1994.tb03995.x. URL https://onlinelibrary.wiley.com/doi/abs/10.1111/j.1365-246X.1994.tb03995.x. _eprint: https://onlinelibrary.wiley.com/doi/pdf/10.1111/j.1365-246X.1994.tb03995.x.

T. Steinke, D. Van Sliedregt, K. Vilella, W. Van Der Wal, and B. Vermeersen. Can a Combination of Convective and Magmatic Heat Transport in the Mantle Explain Io's Volcanic Pattern? *Journal of Geophysical Research: Planets*, 125(12):e2020JE006521, December 2020. ISSN 2169-9097, 2169-9100. doi: 10.1029/2020JE006521. URL https://agupubs.onlinelibrary.wiley.com/doi/10.1029/2020JE006521.

Robert H. Tyler, Wade G. Henning, and Christopher W. Hamilton. TIDAL HEATING IN A MAGMA OCEAN WITHIN JUPITER'S MOON Io. *The Astrophysical Journal Supplement Series*, 218(2):22, June 2015. ISSN 0067-0049. doi: 10.1088/0067-0049/218/2/22. URL https://dx.doi.org/10.1088/0067-0049/218/2/22. Publisher: The American Astronomical Society.

Duncan van Sliedregt. *Volcanism on Io: A Comparison Between the Volcanic Distribution and Tidal Stress*. PhD thesis, Delft University of Technology, Delft, June 2020.

Glenn J. Veeder, Ashley Gerard Davies, Dennis L. Matson, and Torrence V. Johnson. Io: Heat flow from dark volcanic fields. *Icarus*, 204(1):239–253, November 2009. ISSN 0019-1035. doi: 10.1016/j.icarus.2009.06.027. URL https://www.sciencedirect.com/science/article/pii/S0019103509002735.

Glenn J. Veeder, Ashley Gerard Davies, David A. Williams, Dennis L. Matson, Torrence V. Johnson, and Jani Radebaugh. Io: Heat flow from dark paterae. *Icarus*, 212(1):236–261, March 2011. ISSN 0019-1035. doi: 10.1016/j.icarus.2010.09.026. URL https://www.sciencedirect.com/science/article/pii/S0019103510003799.

Glenn J. Veeder, Ashley Gerard Davies, Dennis L. Matson, Torrence V. Johnson, David A. Williams, and Jani Radebaugh. Io: Volcanic thermal sources and global heat flow. *Icarus*, 219(2):701–722, June 2012. ISSN 0019-1035. doi: 10.1016/j.icarus.2012.04.004. URL https://www.sciencedirect.com/science/article/pii/S0019103512001339.

Glenn J. Veeder, Ashley Gerard Davies, Dennis L. Matson, Torrence V. Johnson, David A. Williams, and Jani Radebaugh. Io: Heat flow from small volcanic features. *Icarus*, 245:379–410, January 2015. ISSN 0019-1035. doi: 10.1016/j.icarus.2014.07.028. URL https://www.sciencedirect.com/science/article/pii/S0019103514004138.

Allard Veenstra, Marc Roviara-Navarro, Teresa Steinke, and Wouter van der Wal. Lateral Melt Variations induce Shift in Io's Peak Tidal Heating. page 22, 2024.

David A. Williams, Laszlo P. Keszthelyi, David A. Crown, Jessica A. Yff, Windy L. Jaeger, Paul M. Schenk, Paul E. Geissler, and Tammy L. Becker. Volcanism on Io: New insights from global geologic mapping. *Icarus*, 214(1):91–112, July 2011. ISSN 0019-1035. doi: 10.1016/j.icarus.2011.05.007. URL https://www.sciencedirect.com/science/article/pii/S0019103511001710.

David A. Williams, David M. Nelson, and Moses P. Milazzo. The Io GIS Database 1.0: A Proto-Io Planetary Spatial Data Infrastructure. *The Planetary Science Journal*, 2(4):148, August 2021. ISSN 2632-3338. doi: 10.3847/PSJ/ac097f. URL https://iopscience.iop.org/article/10.3847/PSJ/ac097f/meta. Publisher: IOP Publishing.

F. Zambon, A. Mura, R. M. C. Lopes, J. Rathbun, F. Tosi, R. Sordini, R. Noschese, M. Ciarniello, A. Cicchetti, A. Adriani, L. Agostini, G. Filacchione, D. Grassi, G. Piccioni, C. Plainaki, G. Sindoni, D. Turrini, S. Brooks, C. Hansen-Koharcheck, and S. Bolton. Io Hot Spot Distribution Detected by Juno/JIRAM. *Geophysical Research Letters*, 50(1):e2022GL100597, 2023. ISSN 1944-8007. doi: 10.1029/2022GL100597. URL https://onlinelibrary.wiley.com/doi/abs/10.1029/2022GL100597. _eprint: https://onlinelibrary.wiley.com/doi/pdf/10.1029/2022GL100597.

Ondřej Šebek, Pavel M. Trávníček, Raymond J. Walker, and Petr Hellinger. Dynamic Plasma Interaction at Io: Multispecies Hybrid Simulations. *Journal of Geophysical Research: Space Physics*, 124(1):313–341, 2019. ISSN 2169-9402. doi: 10.1029/2018JA026153. URL https://onlinelibrary.wiley.com/doi/abs/10.1029/2018JA026153. _eprint: https://onlinelibrary.wiley.com/doi/pdf/10.1029/2018JA026153.